TABLE OF CONTENTS

NASA Contractor Report 3283

Simple Turbulence Models and Their Application to Boundary Layer Separation

Alan J. Wadcock

NASA

i

⑦

Simple Turbulence Models and Their Application to Boundary Layer Separation

Alan J. Wadcock
Beam Engineering, Inc.
Sunnyvale, California

NASA

National Aeronautics
and Space Administration

**Scientific and Technical
Information Office**

1980

ii

TABLE OF CONTENTS

ABSTRACT

Measurements in the boundary layer and wake of a stalled airfoil are presented in two coordinate systems - one aligned with the airfoil chord, the other being conventional boundary layer coordinates. The NACA 4412 airfoil is studied at a single angle of attack corresponding to maximum lift, the Reynolds number based on chord being 1.5×10^6. Turbulent boundary layer separation occurred at the 85% chord position. The two-dimensionality of the flow was documented and the momentum integral equation studied to illustrate the importance of turbulence contributions as separation is approached. The assumptions of simple eddy-viscosity and mixing-length turbulence models are checked directly against experiment. Curvature effects are found to be important as separation is approached.

ACKNOWLEDGEMENTS

LIST OF SYMBOLS

c	airfoil chord
C_f	skin friction coefficient, $\tau_w / \frac{1}{2} \rho U_{ref}^2$
C_p	pressure coefficient, $p - p_{ref} / \frac{1}{2} \rho U_{ref}^2$
H	boundary layer shape factor, δ^* / θ
IX,IY	indices referring to processed data mesh
p	static pressure
R	radius of curvature of airfoil surface
R_θ	Reynolds number based on momentum thickness, $U_e \theta / \nu$
u,v,w	velocity components in (x,y) coordinates
U_e	parallel component of velocity at edge of boundary layer
U_{ref}	reference velocity as measured by roof-mounted pitot-static tube
x,y	coordinates normal and parallel to airfoil chord
k	$\frac{1}{2}(\overline{u'^2} + \overline{v'^2} + \overline{w'^2})$
ℓ	mixing length, $(-\overline{u'v'})^{\frac{1}{2}} / (\partial u / \partial y)$
$\overline{q^2}$	$\overline{u'^2} + \overline{v'^2} + \overline{w'^2}$
u,v,w	velocity components in conventional boundary layer coordinates (x,y,z)
x,y	coordinates normal and parallel to local airfoil surface
α	mean streamline direction relative to local airfoil surface, $\tan^{-1}(\bar{v}/\bar{u})$
δ	boundary layer thickness: $y = \delta$ when $\bar{u} = 0.99 U_e$
δ^*	displacement thickness: $\int_0^\infty (1 - \frac{\bar{u}}{U_e}) \, dy$
θ	momentum thickness: $\int_0^\infty \frac{\bar{u}}{U_e} (1 - \frac{\bar{u}}{U_e}) \, dy$
ν	kinematic viscosity, μ / ρ
ν_T	eddy viscosity
ρ	fluid density
τ	shear stress

Suffixes

e   external stream conditions

w   wall conditions

1.0   INTRODUCTION

One of the most detailed investigations of turbulent boundary layer separation was that reported by Schubauer and Klebanoff (Reference 1).   Conventional hot-wire anemometry limited their measurements to the region upstream of separation.   Later, Bidwell (Reference 2) used this data to investigate the importance of turbulence terms in the momentum integral equation.

Wadcock (Reference 3) made measurements in the boundary layer and near wake of a two-dimensional airfoil at a single angle of attack corresponding to maximum lift.   The experiment employed a flying hot-wire to avoid directional ambiguity in the hot-wire signals and so enable measurements to be made in the turbulent boundary layer downstream of separation.   It is believed that these measurements will provide a major test case for development of calculation methods for turbulent flow, and so the above data (in the form of punched   cards) have been filed with NASA-Ames Research Center.   Details of the experimental configuration can be found in Reference 3.

The data takes two essentially distinct forms:

a)   Raw Data

The original output from the hot-wire inversion, consisting of data at discrete points along the flying-hot-wire arcs in a coordinate system based on the wind tunnel axis, was recorded on 14,620 punched cards (85 files, 86 frames, 2 probes).   A tabular description of the card format can be found in Reference 3.   The raw data are thus defined at points which are awkardly placed.   Further processing was therefore performed.

b)   Processed Data

One objective was to use interpolation to redefine the data on a rectangular grid which is sufficiently fine to satisfy the analyst without driving the data beyond their real accuracy.   Mostly for convenience in

describing the airfoil surface the grid in question is aligned with the air-
foil chord. A further objective was to lay a foundation for the calculation
of spatial derivatives. These final processed data were recorded on 29,195
punched cards. Because the passage from raw to processed data was not only
tedious but expensive, we expect most users will be willing to begin with the
processed version of the data (see References 4 and 5). Reference 5 contains
a partial listing of the processed data.

The rectangular grid used for the processed data is aligned with the air-
foil chord. The method of interpolation and smoothing is detailed in Reference
3. The mesh size is 1 cm in the chordwise direction and 0.2 cm in the cross-
flow direction. Integer grid indices for the mesh, IX and IY, are related
to the coordinates x and y of Figure 1 by

$$IX = 1 + (x - 6.86)$$

$$IY = 1 + 5(y + 12.41)$$

where x and y are in centimeters. IY ranges from 1 to 296 and IX from 1 to
175 thereby documenting the wake flow for one chord length downstream of the
airfoil trailing edge.

2.0   PROCESSED DATA

The processed data is presented in the form of contour plots in Figures
2, 3 and 4. Figure 2 is a plot of the intermittency factor (fraction of the
time that the flow is turbulent at a given position in space) in the boundary
layer and near wake. The intermittency is close to unity over a substantial
part of the boundary layer. To a lesser extent the same is true for the near
wake. Figure 3 presents the mean velocity components normal and parallel to
the airfoil chord. The reverse-flow region is clearly visible starting at
$x/c \simeq 0.85$ and extending to $x/c \simeq 1.07$. The mean reverse-flow velocity in

the recirculation region is less than 20% of the free-stream velocity. Figure 4 presents data on the three double correlations $\overline{u'u'}$, $\overline{u'v'}$, and $\overline{v'v'}$. In the boundary layer, as expected, velocity fluctuations parallel to the chord are very much larger than those normal to the wall. Downstream of the airfoil trailing edge, however, fluctuations in the two velocity components soon become comparable. The contour $\overline{u'v'} = 0$ appears to emanate from close to the airfoil trailing edge, far from the apparent separation point as indicated by the mean velocity data. The explanation lies in the fact that at separation the shear stress is zero only when evaluated in boundary layer coordinates (i.e., normal and parallel to the local airfoil surface).

3.0 TWO-DIMENSIONALITY

Before too much effort was expended in considering the success or failure of turbulence models in predicting the separated flow around the airfoil in question, it was necessary to document the two-dimensionality of the flow as fully as possible. Static pressure measurements on the airfoil surface (see Figure 5) and total pressure measurements through the wake approximately 1½ chords downstream of the airfoil trailing edge (see Figure 6) at three spanwise stations indicate excellent two-dimensionality. However, it is well known that pressure measurements are insensitive indicators of three-dimensionality--a small lateral pressure gradient can result in substantial spanwise motion.

The density of the data made available under the name "processed data" allows the computation of spatial gradients quite readily. It is instructive to test the two-dimensionality of the flow by examining the equation for conservation of mass:

$$\frac{\partial \bar{u}}{\partial x} + \frac{\partial \bar{v}}{\partial y} = -\frac{\partial \bar{w}}{\partial z}$$

Clearly, if the left-hand side of the above equation is zero everywhere, then the flow is two-dimensional. If it is non-zero, then there will be cross-flow.

Before computing $\partial\bar{u}/\partial x$ and $\partial\bar{v}/\partial y$ we need some measure of the reliability of the spatial gradients. This can be obtained by considering the vorticity

$$\zeta = \frac{\partial\bar{v}}{\partial x} - \frac{\partial\bar{u}}{\partial y}$$

3.1   VORTICITY

In the external flow (i.e., outside both the boundary layer and wake) the flow is irrotational. The vorticity must be zero even if the flow is three-dimensional. This enables one to assign some sort of confidence level to spatial gradients of the mean velocity. Outside the boundary layer and wake such gradients are naturally much smaller than inside. However, useful information may be gathered from such an investigation.

Working in the coordinate system based on the airfoil chord data is presented in Figures 7, 8 and 9 along lines of constant x.

(a)   Through the boundary layer at IX = 50 (upstream of separation, x/c = 0.620)

(b)   Through the boundary layer at IX = 75 (downstream of separation, x/c = 0.897)

(c)   Through the wake at IX = 100 (x/c = 1.175).

Spatial gradients are computed by simple differencing of the processed data (see Reference 3) which is available every 1 cm in x and every 0.2 cm in y. Just as all velocity components are normalized with the tunnel reference velocity U_{ref}, all spatial gradients are made non-dimensional by means of the airfoil chord, c. Because of the 5:1 ratio in grid step size in the arrays

containing the mean velocity data, gradients in the y-direction show five times the scatter displayed by the x-derivatives, i.e., x-derivatives appear much smoother. The absolute accuracy of the data is within 2% for the dimensionless mean velocity components, but it is much harder to assign a similar figure to the spatial gradients. Examination of Figure 9 for $x/c = 1.175$ shows that $\partial \bar{u}/\partial y$ bounces around somewhat on one side of the wake. This scatter is directly traceable to the raw data (see Reference 3) and unfortunately persisted throughout the smoothing and interpolation process. This problem is only present in the wake and does not appear in the boundary layer. The maximum scatter in the y-derivatives is therefore ± 1. The x-derivatives are much smoother. From Figures 7, 8, and 9 it appears that the vorticity as calculated from $\partial \bar{v}/\partial x - \partial \bar{u}/\partial y$ is sufficiently close to zero in the external flow that the spatial gradients are reliable.

3.2   CONSERVATION OF MASS

Conservation of mass requires, for a general three-dimensional flow

$$\frac{\partial \bar{u}}{\partial x} + \frac{\partial \bar{v}}{\partial y} + \frac{\partial \bar{w}}{\partial z} = 0$$

We already have some degree of confidence in the spatial derivatives outside the boundary layer and wake. If we can assume that these gradients are equally reliable inside the boundary layer and wake (where they are necessarily much larger) then we can apply the above equation in the form

$$\frac{\partial \bar{u}}{\partial x} + \frac{\partial \bar{v}}{\partial y} = - \frac{\partial \bar{w}}{\partial z}$$

to obtain some measure of the two-dimensionality of the flow (see Figures 10, 11, and 12). Despite the difficulties inherent in the differentiation of experimental data, downstream of the airfoil trailing edge $\partial \bar{w}/\partial z$ is zero within

9

reasonable limits considering the separately large values of $\partial\bar{u}/\partial x$ and $\partial\bar{v}/\partial y$.
At station 75 however, $\partial\bar{w}/\partial z$ exhibits a departure typical of most boundary
layer stations indicating some cross-flow or divergence. Absence of ex-
perimental skin-friction data makes a momentum balance difficult to perform.
Lack of an extensive logarithmic region in the velocity profile makes a
Clauser plot for C_f unprofitable. It is therefore difficult to assess the
degree of three-dimensionality with any certainty.

4.0   DATA IN BOUNDARY LAYER COORDINATES

Data in conventional boundary layer coordinates (normal and parallel to
the local airfoil surface) were obtained approximately every 1 cm along the
airfoil surface by interpolation in the proc ised data and rotation into the
new coordinate system (see Figure 3).

Figure 13 shows that the intermittency is close to unity over much of the
boundary layer. Intermittency is a scalar quantity and hence is independent
of the coordinate system chosen for presentation. Figure 13 and Figure 2 are
therefore essentially the same. The mean velocity components $\bar{u}$ and $\bar{v}$ are
shown in Figures 14 and 15. Figure 14 indicates that separation occurs close
to station 70. The reverse-flow velocity is everywhere less than 20% of the
free-stream velocity. Figure 16 presents the ratio of the mean velocity com-
ponents $\bar{v}/\bar{u}$. It should be recalled that one of the Prandtl boundary layer
assumptions is $\bar{v} \ll \bar{u}$. Perhaps a reasonable limit on the validity of such an
assumption would be $\bar{v}/\bar{u} = 0.1$. As can be seen from Figure 16 such a value
is reached well ahead of separation. Figure 17 presents the same data in a
slightly different form. This figure shows the angle that the mean flow makes
with the local airfoil surface. Note that for $\bar{v}/\bar{u} = 0.1$, $\tan^{-1}(\bar{v}/\bar{u}) \simeq$
6 degrees so the flow does not have to depart from being parallel to the wall
by very much to invalidate the assumption $\bar{v} \ll \bar{u}$.

Figures 18, 19 and 20 present the three Reynolds stress terms $\overline{u'u'}$, $\overline{u'v'}$ and $\overline{v'v'}$. As can be readily seen, downstream of separation very high turbulence levels are encountered with $\sqrt{\overline{u'^2}}/U_{ref}$ as high as 30%. Schubauer and Klebanoff (Reference 1) report much lower turbulence levels at separation, possibly due to poor instrument response (the time constants for their hot wires were approximately 0.002 seconds). Figure 19 shows that the corresponding velocity fluctuations in the normal direction are much smaller as expected. Figure 20 presents the Reynolds shear stress. The maximum shear stress is seen to occur first near the surface and move progressively outwards with increasing downstream distance. At station 70 $\overline{u'v'}$ is close to zero near the wall as expected (cf, Figures 3 and 4). However, starting slightly ahead of separation, $\overline{u'v'}$ becomes positive in the outer part of the shear layer.

At first sight this was surprising, but a similar phenomenon has previously been observed with curved shear layers. Streamline curvature in the plane of the mean shear is known to produce surprisingly large changes in the turbulence structure of shear layers. To understand this effect, a short discussion is appropriate. A flow is said to be stable if, on displacement, a fluid particle is prevented from further displacement by a net restoring force. For flows over convex surfaces the centrifugal force is balanced by an inward pressure gradient. If a fluid particle is displaced outward across mean streamlines into regions of higher mean velocity, the centrifugal force on the fluid particle will be less than the new mean normal pressure gradient resulting in a restoring force. Similarly, if the fluid particle is displaced inward, a net outward restoring force results. Thus convex boundary layer flows exert a stabilizing influence on turbulent momentum exchange resulting in a decrease in the interchange of both momentum and energy.

11

The direct effect of curvature on the Reynolds stresses was measured by So and Mellor (Reference 6) for a turbulent boundary layer on a convex wall. In their measurements the boundary layer was first developed on a flat surface and then passed to a convex surface; the R/δ ratio was about 12. The stabilizing effect of curvature was immediately evident resulting in the virtual disappearance of the turbulence in the outer layer. The ability of turbulence to produce shear stress was reduced by the stabilizing effect of curvature and a shear-stress profile that vanished in a region where the velocity gradient was still substantial was measured. A corresponding rapid decrease in skin-friction coefficient was also observed.

A careful scrutiny of the data of So and Mellor at the most downstream stations reveals not simply the suppression of Reynolds shear stress but indeed a sign reversal for $\overline{u'v'}$ in the outer half of the boundary layer. Their measurements proceeded some 24 boundary layer thicknesses downstream from the start of wall curvature in a flow of essentially zero pressure gradient with R/δ constant at about 12. It is not difficult to assume that if the measurements had continued downstream a more noticeable effect may have been visible. The present data is the result of the combined effects of streamwise pressure gradient and continuously variable curvature parameters R/δ. R/δ is found to vary from 100 at the earliest stations for which boundary layer data is available to 20 at the airfoil trailing edge. The adverse external pressure gradient obscures the direct interpretation of curvature effects however. For example, the increased turbulent activity normally associated with the approach to separation apparently more than compensates for the stabilizing effect of curvature in the outer part of the boundary layer. No reduction in turbulent activity in the outer part of the layer is observed.

Thus we have a region in which $\partial \bar{u}/\partial y$ and the Reynolds shear stress $-\rho \overline{u'v'}$ are of opposite sign. The turbulent energy production term $-\overline{u'v'}\, \partial \bar{u}/\partial y$ will have a negative value in this region. This implies that locally the energy of the mean flow is being increased at the expense of the turbulence.

It is not the absolute values of the turbulent intensities but rather their ratio that provides useful information about changes in turbulence structure. Figure 21 presents the shear stress normalized with the turbulent energy and Figure 22 presents the same data normalized with the rms velocity fluctuations. $-\overline{u'v'}/q^2$ is a simple measure of the efficiency of the turbulence in producing shear stress. For a flat plate boundary layer its value is about 0.18 over most of the boundary layer decreasing rapidly near the edge of the layer. Measurements by So and Mellor (Reference 6) show that convex curvature lowers this value and, instead of going to zero at the edge of the velocity layer, it goes to zero at about half the boundary layer thickness. If we assume $\overline{w'w'} \simeq \frac{1}{2}\left(\overline{u'u'}+\overline{v'v'}\right)$ then $-\overline{u'v'}/q^2 \simeq -\left(\frac{2}{3}\right)\overline{u'v'}/\left(\overline{u'u'}+\overline{v'v'}\right)$. If the data presented in Figure 21 are examined in detail, we find that $-\overline{u'v'}/q^2$ is essentially constant across the boundary layer for the early stations. For example, at station 55 $-\overline{u'v'}/q^2$ takes the value 2/3 of 0.11 and at station 60 the value 2/3 of 0.08, constant over the inner 75% of the layer. Downstream of separation, of course, the character of this parameter is completely different due to the sign change associated with the Reynolds shear stress that occurs in the middle of the layer.

For the flat plate boundary layer the correlation coefficient $-\overline{u'v'}/\sqrt{\overline{u'^2}}\sqrt{\overline{v'^2}}$ is found to assume a constant value of 0.5 over the inner 3/4 of the boundary layer thickness, decreasing rapidly to zero at the edge of the layer. Convex curvature is found to reduce both the lateral extent of the region of constant

13

correlation coefficient and also the value of the coefficient (Reference 6). Figure 22 shows that at the earliest boundary layer stations the correlation coefficient is already down to 0.4 and as separation is approached this value decreases rapidly. The assumption of constant correlation coefficient through the boundary layer also steadily becomes worse.

Figure 23 presents data on the growth of the boundary layer thickness δ and includes information on the variation of the external velocity U_e at the edge of the boundary layer. The boundary layer thickness increases rapidly as separation is approached, the growth rate assuming a constant value $\frac{d\delta}{dx} \simeq 0.32$.

Figure 24 shows the development of the velocity profile every fifth station along the airfoil surface. At the earliest station for which boundary layer data is available (station 50, $x/c = 0.620$) a substantial velocity defect exists over much of the layer indicating the proximity of separation. Figure 25 presents the velocity distribution through the boundary layer at each of the above stations the normalizing velocity being the local external velocity in each case.

Figure 26 displays the integral parameters δ^*, Θ and $H = \delta^*/\Theta$, where the plane wall definitions were used in evaluating the integral thickness. Downstream of separation the displacement thickness δ^* is seen to grow linearly with distance along the airfoil surface, $d\delta^*/dx \simeq 0.24$. At separation the shape factor H is approximately 3.6. Schubauer and Klebanoff quote a shape factor close to 2.7 at separation. Table 1 lists δ^*, Θ and H at a few select stations. No data is at present available on the surface shear stress distribution.

5.0 THE REYNOLDS EQUATIONS

The motivation behind presentation of data in boundary layer coordinates was the term-by-term examination of the time-mean Navier Stokes equations in order to investigate the validity of the Prandtl boundary-layer assumptions in the vicinity of separation.

The Navier Stokes equations for a two-dimensional flow in which the viscosity and density are assumed constant and the body forces are negligible are:

$$\frac{\partial u}{\partial t} + u\frac{\partial u}{\partial x} + v\frac{\partial u}{\partial y} = -\frac{1}{\rho}\frac{\partial p}{\partial x} + \nu\left(\frac{\partial^2 u}{\partial x^2} + \frac{\partial^2 u}{\partial y^2}\right) \tag{1}$$

$$\frac{\partial v}{\partial t} + u\frac{\partial v}{\partial x} + v\frac{\partial v}{\partial y} = -\frac{1}{\rho}\frac{\partial p}{\partial y} + \nu\left(\frac{\partial^2 v}{\partial x^2} + \frac{\partial^2 v}{\partial y^2}\right) \tag{2}$$

The associated continuity equation is

$$\frac{\partial u}{\partial x} + \frac{\partial v}{\partial y} = 0 \tag{3}$$

By resolving the instantaneous values into mean and fluctuating components, by considering the mean flow steady and taking a long-time average of the fluctuating components and by using the continuity equation, equations (1) and (2) may be written as

$$\bar{u}\frac{\partial \bar{u}}{\partial x} + \bar{v}\frac{\partial \bar{u}}{\partial y} + \frac{\partial}{\partial x}(\overline{u'u'}) + \frac{\partial}{\partial y}(\overline{u'v'}) = -\frac{1}{\rho}\frac{\partial \bar{p}}{\partial x} + \nu\left(\frac{\partial^2 \bar{u}}{\partial x^2} + \frac{\partial^2 \bar{u}}{\partial y^2}\right) \tag{4}$$

$$\bar{u}\frac{\partial \bar{v}}{\partial x} + \bar{v}\frac{\partial \bar{v}}{\partial y} + \frac{\partial}{\partial x}(\overline{u'v'}) + \frac{\partial}{\partial y}(\overline{v'v'}) = -\frac{1}{\rho}\frac{\partial \bar{p}}{\partial y} + \nu\left(\frac{\partial^2 \bar{v}}{\partial x^2} + \frac{\partial^2 \bar{v}}{\partial y^2}\right) \tag{5}$$

15

Considering the Prandtl boundary-layer assumptions valid ($\frac{\partial}{\partial x} \ll \frac{\partial}{\partial y}$, $\bar{v} \ll \bar{u}$),

$$\bar{u}\frac{\partial \bar{u}}{\partial x} + \bar{v}\frac{\partial \bar{u}}{\partial y} + \frac{\partial}{\partial x}(\overline{u'u'}) + \frac{\partial}{\partial y}(\overline{u'v'}) = -\frac{1}{\rho}\frac{\partial \bar{p}}{\partial x} + \nu\frac{\partial^2 \bar{u}}{\partial y^2} \tag{6}$$

$$\frac{\partial}{\partial y}(\overline{v'v'}) = -\frac{1}{\rho}\frac{\partial \bar{p}}{\partial y} \tag{7}$$

Combining the above two equations,

$$\bar{u}\frac{\partial \bar{u}}{\partial x} + \bar{v}\frac{\partial \bar{u}}{\partial y} + \frac{\partial}{\partial x}(\overline{u'u'} - \overline{v'v'}) = U_e\frac{dU_e}{dx} + \frac{1}{\rho}\frac{\partial \tau}{\partial y} \tag{8}$$

where U_e is the velocity at the edge of the boundary layer and $\tau = \tau_L + \tau_T$; $\tau_L = \mu\frac{\partial \bar{u}}{\partial y}$, $\tau_T = -\rho\overline{u'v'}$.

The above equations were written for flow along a flat wall. For two-dimensional flow along a curved wall we can write the corresponding equations in a curvilinear orthogonal system of co-ordinates whose **x**-axis is parallel to the wall, the **y**-axis being perpendicular to it (see Figure 1). With the assumptions that the boundary layer thickness is small compared with the radius of curvature of the wall and viscous terms are small compared with inertial terms (i.e., high Reynolds Number) we obtain

$$\frac{\partial u}{\partial t} + u\frac{\partial u}{\partial x} + v\frac{\partial u}{\partial y} + \frac{uv}{R} = -\frac{1}{\rho}\frac{\partial p}{\partial x} \tag{1a}$$

$$\frac{\partial v}{\partial t} + u\frac{\partial v}{\partial x} + v\frac{\partial v}{\partial y} - \frac{u^2}{R} = -\frac{1}{\rho}\frac{\partial p}{\partial y} \tag{2a}$$

16

$$\frac{\partial u}{\partial x} + \frac{\partial v}{\partial y} + \frac{v}{R} = 0 \qquad\qquad (3a)$$

For the flow under consideration the curvature terms are important. The object of the following discussion is to establish the importance of individual terms in the time-mean version of the above equations, namely

$$\bar{u}\frac{\partial \bar{u}}{\partial x} + \bar{v}\frac{\partial \bar{u}}{\partial y} + \frac{\partial}{\partial x}\left(\overline{u'u'}\right) + \frac{\partial}{\partial y}\left(\overline{u'v'}\right) + \left(\frac{\bar{u}\bar{v} + 2\overline{u'v'}}{R}\right) = -\frac{1}{\rho}\frac{\partial p}{\partial x} \qquad (4a)$$

$$\bar{u}\frac{\partial \bar{v}}{\partial x} + \bar{v}\frac{\partial \bar{v}}{\partial y} + \frac{\partial}{\partial x}\left(\overline{u'v'}\right) + \frac{\partial}{\partial y}\left(\overline{v'v'}\right) - \left(\frac{\bar{u}\bar{u} + \overline{u'u'} - \overline{v'v'}}{R}\right) = -\frac{1}{\rho}\frac{\partial p}{\partial y} \qquad (5a)$$

Each term on the left-hand side of equations (4a) and (5a) has been evaluated at three streamwise positions on the airfoil surface:

Station	Description
55	Upstream of separation
70	Close to separation
80	Downstream of separation

Spatial gradients were estimated by simple differencing in data stored at grid locations with a mesh size of approximately 1 cm by 0.2 cm in the orthogonal directions x and y, parallel and normal to the local airfoil surface respectively.

Figures 27, 28 and 29 present a study of individual terms in the y-momentum equation (equation 5a) at each of the above three stations $x/c = 0.675$,

17

0.842 and 0.952. It is clear from all three figures that curvature terms are important at all stations along the surface of the wing. The usual neglect of the terms $\bar{u}\frac{\partial \bar{v}}{\partial x}$ and $\bar{v}\frac{\partial \bar{v}}{\partial y}$ from the y-momentum equation is seen to have little justification. Each term is separately quite large and comparable with the term that is retained, namely $\frac{\partial}{\partial y}(\overline{v'v'})$. The one term that can quite safely be neglected throughout the boundary layer is $\frac{\partial}{\partial x}(\overline{u'v'})$.

At the outside edge of the boundary layer $\frac{\partial p}{\partial y} \simeq 0$ for stations 55 and 70 whereas downstream of separation (station 80) this is not the case. Neglecting turbulent contributions to the momentum equation, equation (5a) becomes

$$\bar{u}\frac{\partial \bar{v}}{\partial x} + \bar{v}\frac{\partial v}{\partial y} - \frac{\bar{u}\bar{u}}{R} = -\frac{1}{\rho}\frac{\partial p}{\partial y}$$

or

$$\frac{\partial p}{\partial y} = \rho\,\bar{u}^2\left[\frac{1}{R} - \frac{\partial}{\partial x}\left(\bar{v}/\bar{u}\right)\right].$$

Large transverse pressure gradients are thus to be expected in regions of rapid streamline curvature, e.g. close to separation where the mean streamlines are closed. However, in the recirculation region the mean velocity is low and hence large transverse pressure gradients are not encountered. The quantity in the square brackets in the above equation represents the difference between the mean streamline curvature and the local curvature of the wall. Thus we see from Figures 27 and 28 that the external flow is moving parallel to the wall at stations 55 and 70. Downstream of separation however, Figure 29 indicates that the external flow is no longer parallel to the local airfoil surface indicating that the shear layer has simply peeled off. Examination of Figures 27, 28 and 29 shows that the largest pressure difference across the layer for the three stations considered occurs at station 80. This is

18

the result of having both the largest transverse pressure gradient and the thickest layer present at this station. Integration of $\frac{\partial p}{\partial y}$ across the layer at this station yields a value for $\Delta C_p = C_{p_e} - C_{p_w}$ of approximately 0.07.

Figures 30 , 31 and 32 refer to individual terms in the x-momentum equation (equation 4a) evaluated at stations 55, 70 and 80 corresponding to x/c = 0.675, 0.842 and 0.952. Figure 30 shows that ahead of separation (station 55) a large adverse pressure gradient is present throughout the boundary layer. Figure 32 shows that at station 80, downstream of separation, $\frac{\partial p}{\partial x} > 0$ in the outer half of the layer whereas close to the wall $\frac{\partial p}{\partial x} < 0$. This is entirely consistent with the fact that fluid close to the wall is moving upstream at this station. As fluid moves upstream it must move into a region of increasing pressure in order to be brought to rest at the separation point. Thus there should be a favorable streamwise pressure gradient close to the wall at station 80. The streamwise pressure gradient at the wall has also been evaluated from the surface pressure distribution shown in Figure 5. This information is also shown plotted in Figures 30, 31 and 32 for comparison. Note that at the wall, equation (4a) reduces to

$$ -\frac{1}{\rho} \left. \frac{\partial p}{\partial x} \right)_w = \frac{\partial}{\partial y} \left(\overline{u'v'} \right) $$

so that comparison between the pressure gradient evaluated from the flying-hot-wire measurements using equation (4a) and that computed from surface pressure measurements is really only a comparison between the streamwise gradient of the surface pressure and the normal gradient of the Reynolds shear stress.

19

6.0   THE MOMENTUM INTEGRAL EQUATION

Figure 33 examines individual terms in the momentum integral equation, neglecting contributions from turbulent fluctuations:

$$\frac{\tau_w}{\rho U_e^2} = \frac{d\theta}{dx} + (H+2)\frac{\theta}{U_e}\frac{dU_e}{dx}$$

If the above equation is used to describe the variation of the wall shear stress τ_w, as we move downstream and approach separation τ_w is found to increase (at least initially). This is clearly incorrect as the boundary layer is growing in an adverse pressure gradient (see Figure 23 for $U_e(x)$) and so τ_w should fall monotonically as separation is approached. This problem has been encountered by other researchers (see reference 2). Downstream of station 72 $\tau_w < 0$ indicating reversed flow --- cf mean velocity data shown in Figure 14. The agreement appears fortuitous considering the indicated behavior of τ_w ahead of separation.

Following Bidwell (Reference 2), the momentum integral equation can be written

$$\frac{\tau_w}{\rho U_e^2} = \frac{d\theta}{dx} + (H+2)\frac{\theta}{U_e}\frac{dU_e}{dx} - \frac{1}{U_e^2}\int_0^\delta \frac{\partial}{\partial x}(\overline{u'u'})\,dy$$

$$+ \frac{1}{U_e^2}\int_0^\delta \int_0^y \frac{\partial}{\partial x}\left(\frac{\partial}{\partial x}(\overline{u'v'}) + \frac{\partial}{\partial y}(\overline{v'v'})\right)dy\,dy - \frac{\delta}{U_e^2}\int_0^\delta \frac{\partial^2}{\partial x^2}(\overline{u'v'})\,dy$$

where curvature effects have been neglected and only turbulent contributions

20

to $\frac{\partial \hat{p}}{\partial y}$ retained in equation (5a). Contributions to the momentum integral equation from the above turbulence terms were evaluated at a limited number of stations. The results are presented in Table 2. Clearly the most significant contribution comes from the streamwise derivative of $\overline{v'u'}$. This term only involves the first derivative of $\overline{v'u'}$ and hence can be determined relatively accurately from the experimental data. Contributions from other terms are much smaller, although still significant, and rely on the calculation of second derivatives---their accuracy is therefore diminished. The cumulative effect of these turbulent contributions is insufficient to account for the growth of $\tau_w(x)$. Assuming that the mean flow is indeed two-dimensional this can only be due to the omission of curvature terms from the equations of motion and the neglect of mean convective terms in the y-momentum equation.

7.0 TURBULENCE MODELS

There are two essential problems associated with Reynolds averaging (Reference 7). First, since the Reynolds stresses are unknowns, Reynolds averaging leads to a set of equations with more variables than equations. An attempt to obtain equations for the Reynolds stresses by successive multiplication of the Navier Stokes equations followed by time averaging leads to a hierarchy of equations in which, for example, $\overline{u'v'}$ depends on terms of the form $\overline{u'u'v'}$ and so on. The hope in using Reynolds averaging lies with the possibility of closing the resulting sequence of equations by a physical or at least a statistical argument. This is the so-called closure problem.

The second problem with Reynolds averaging is related to the usefulness of such averaging. Recently it has become clear that Reynolds averaging is not as obviously useful as has previously been thought. Time-resolved measurements of the statistical properties of such terms as $\overline{u'v'}$ show, at least in some

21

cases, a nearly bi-modal probability distribution; the dimensionless coefficient $-\overline{u'v'}\big/\sqrt{\overline{u'^2}}\sqrt{\overline{v'^2}}$ is found to be zero for stretches of time interrupted by bursts in which it is unity; its mean value, the correlation coefficient, is of the order of 0.5. The physical significance of the mean value of a variable fluctuating in this fashion is at least questionable.

If the viscous shear and normal turbulent stress terms are neglected in equation (6) and the resulting equation combined with the time-mean of equation (3) we have a system of equations that can be solved for any given external pressure gradient, provided something can be said about the turbulent shear stress $-\rho\,\overline{u'v'}$. The primary objective of all turbulence models is therefore a description of the Reynolds shear stress.

The simplest models relate the turbulent shear stress uniquely to the mean flow conditions at each point. Since these models require only algebraic expressions they have enjoyed prolonged popularity. All models of this class use the eddy-viscosity concept of Boussinesq:

$$- \overline{u'v'} \;=\; \nu_T \frac{\partial \bar{u}}{\partial y}$$

where ν_T is the eddy viscosity. The two most familiar examples of this class are distinguished by the way in which ν_T is calculated.

a) Constant-Eddy-Viscosity Model, $\nu_T = c\,\delta\,(U_{Max} - U_{Min})$.

All quantities on the right-hand side of this equation, apart from c, may be functions of the longitudinal distance x; ν_T is supposed uniform over any cross-section.

b) Mixing Length Hypothesis, $\nu_T = \ell^2 \dfrac{\partial \bar{u}}{\partial y}$.

The mixing length ℓ is usually taken as proportional to δ. This method is still the basis of many calculations of the turbulent boundary layer which are carried out today.

For many boundary layer flows, Prandtl's mixing length hypothesis works surprisingly well. The spreading rate, as well as velocity profile, can be predicted satisfactorily. However, the constants involved must vary with the problem considered. This lack of universality is an indication that the underlying model of turbulence lacks some important features of real flows.

Figure 34 plots the ratio $-\overline{u'v'}/\frac{\partial \overline{u}}{\partial y}$ against y/δ for four stations ahead of separation. Clearly, the closer the approach to separation, the less accurate the assumption $\nu_T = constant$ becomes. The constant-eddy-viscosity model assumes that ν_T scales with δ and U_e; for example, $\nu_T = \alpha \delta^* U_e$ where $\delta^* = \delta^*(x)$, $U_e = U_e(x)$ and α is a constant. Figure 35 shows that there is a substantial decrease in $\nu_T/U_e \delta^*$ as separation is approached. Galbraith and Head (Reference 8) found the same to be true for the experimental data of Schubauer and Spangenberg, Flow B (Reference 9). They found $(\nu_T/U_e\delta^*)_{MAX}$ decreased from approximately 0.018 to 0.007 as separation was approached. The present data apparently starts where the Schubauer and Spangenberg data finishes since $(\nu_T/U_e\delta^*)_{MAX.}$ is already down to 0.007 at the earliest station for which boundary layer data is available. Various flows were examined by Galbraith and Head revealing values for $(\nu_T/U_e\delta^*)_{MAX}$ as high as 0.028. A particular value for $(\nu_T/U_e\delta^*)_{MAX}$ may be typical for a given flow but is apparently highly dependent on the state of equilibrium of the flow.

As mentioned above, Figure 34 shows that as separation is approached, the assumption of constant eddy viscosity across the boundary layer becomes less accurate. Examination of Figures 14 and 20 reveals that downstream of separation the constant-eddy-viscosity model fails completely. Whereas $\partial \overline{u}/\partial y$ is positive throughout the boundary layer (apart from a very thin layer close to the wall) $-\overline{u'v'}$ is positive close to the wall and negative in the outer

23

half of the layer. The ratio $-\overline{u'v'}\left/\dfrac{\partial \bar{u}}{\partial y}\right.$ changes sign across the boundary layer and is thus far from being constant. It therefore appears that the constant-eddy-viscosity model has limited success well ahead of separation, but as separation is approached the model is unrealistic.

If we examine the mixing length hypothesis the story is somewhat similar. The mixing length is given by $l^2 = -\overline{u'v'}\left/\dfrac{\partial \bar{u}}{\partial y}\left|\dfrac{\partial \bar{u}}{\partial y}\right|\right.$. Figure 36 shows that at the earliest stations the assumption $l = constant$ may not be too bad, but the assumption gets progressively worse as separation is approached. The mixing length is assumed to scale with δ for the outer part of the boundary layer. Figure 37 shows that this assumption is valid well ahead of separation. Close to the wall the mixing length is generally assumed to be described by $l = \varkappa y \ (\varkappa = 0.4)$. The agreement is satisfactory although insufficient data is available close to the wall to be conclusive. For many boundary layer flows $l/\delta \approx 0.10$ for $y/\delta \geq 0.25$ (see Reference 8). However, for the early boundary layer stations a typical value for l/δ is 0.05, half the above value. Galbraith and Head (Reference 8) also noticed a decrease in l/δ for the outer part of the layer as separation is approached. Downstream of separation the mixing length model fails for essentially the same reason the constant-eddy-viscosity model failed. Once again, in boundary layer coordinates, $\dfrac{\partial \bar{u}}{\partial y}$ is positive throughout the layer (except very close to the wall) whereas $\overline{u'v'}$ changes sign in the middle of the layer. A negative value for the ratio $-\overline{u'v'}\left/\dfrac{\partial \bar{u}}{\partial y}\left|\dfrac{\partial \bar{u}}{\partial y}\right|\right.$ is not consistent with the physical model.

One of the more successful turbulence models employs the turbulent kinetic energy equation and assumes that the shear stress $\tau_T = -\rho\overline{u'v'}$ is closely related to the turbulence kinetic energy $\frac{1}{2}\rho\left(\overline{u'^2} + \overline{v'^2} + \overline{\omega'^2}\right)$. Townsend proposed that the ratio $\overline{u'v'}$ to $k = \frac{1}{2}\left(\overline{u'^2} + \overline{v'^2} + \overline{\omega'^2}\right)$ might be a universal

constant. Bradshaw employed this assumption with great success as part of a calculation procedure for attached boundary layers. For many flows, however, the underlying assumption is not realistic. Often the shear stress vanishes where the turbulence kinetic energy k remains finite, or, as in the case for round jets, where k has its maximum value. Bradshaw defines the Reynolds shear stress by $-\overline{u'v'} = a_1 \overline{q^2}$ where $\overline{q^2} = (\overline{u'^2} + \overline{v'^2} + \overline{\omega'^2})$ and assigns the value 0.15 to a_1 . Examination of Figure 21 shows that this is reasonable only for the very earliest of boundary layer stations. As separation is approached the assumption becomes less accurate.

Yet another model includes the proposal $-\overline{u'v'} = \nu_T \frac{\partial \bar{u}}{\partial y}$ where the eddy viscosity is allowed to vary through the layer according to $\nu_T = c k^{\frac{1}{2}} L$ and $k = \frac{1}{2} (\overline{u'^2} + \overline{v'^2} + \overline{\omega'^2})$ is calculated from a differential equation and the length scale from an empirical algebraic expression. This model suffers from the same problem the constant-eddy-viscosity model has---namely, down-stream of separation $\overline{u'v'}$ passes through zero in the middle of the boundary layer where $\frac{\partial \bar{u}}{\partial y}$ is far from zero.

It should be emphasized at this point that the major problem with all the above turbulence models is associated with the change in sign of the Reynolds shear stress in the outer part of the boundary layer downstream of separation. If the hot-wire data is examined in the original coordinate system of Figure 4 (axes normal and parallel to the airfoil chord), this problem no longer exists. As a result, $\alpha = \nu_T / u_e \delta^*$ is more nearly constant across the layer, even downstream of separation, although the problem of predicting the value of α remains unsolved. Perhaps this is an indication that a turbulence model may fail because of an inappropriate choice of coordinate system. Close to separation, boundary layer coordinates are perhaps inappropriate anyway. An attractive alternative coordinate system that merits attention is orthogonal to the local mean streamlines.

Bradshaw (Reference 10) discusses the effect of "extra" strain rates (i.e., other than a simple shear $\frac{\partial \bar{u}}{\partial y}$). For a small extra strain rate e the Reynolds stresses are expected to change by a factor $F = 1 + \beta \cdot \frac{e}{\partial \bar{u}/\partial y}$ where β varies from case to case but is of order 10. The rate of strain is defined as small if $e/(\partial \bar{u}/\partial y)$ is numerically less than 0.05 so that $0.5 < F < 1.5$. Outside this range a linear correction factor like F cannot be trusted. For a thin curved shear layer the extra rate of strain is $e = \frac{\partial v}{\partial x}$ in (x,y) coordinates or $e = -U/(y+R)$ in (x,y) coordinates. To account for the observed change in sign of the Reynolds shear stress requires F to change sign, which takes us outside the range of validity of the model.

8.0   CONCLUSIONS

A shortage of experimental data limits the development of turbulence models. The determination of the most economical computational model for the prediction of subsonic flows separating from solid surfaces remains a problem of considerable interest. Numerical solution of the full Navier Stokes equations requires considerable computer time and thus provides motivation for considering the range of applicability of methods based on more approximate forms of the governing equations.

The richness of the experimental data was illustrated by the use of contour plots. The reliability of spatial gradients was also documented. Individual terms in the time-mean Navier Stokes equations were examined to determine their relative importance. In particular, the usual simplification of the y-momentum equation to $\frac{\partial p}{\partial y} = -\rho \overline{v'^2}$ was shown to be unjustifiable close to separation.

Contributions to the momentum integral equation from turbulence terms were shown to be essential as separation is approached. The form of the

26

momentum integral equation used by Bidwell failed to represent the behavior of the wall shear stress even with turbulence contributions included. This was attributed to the neglect of certain terms from the y-momentum equation, terms which are large close to separation.

Eddy-viscosity and mixing-length turbulence models are closely-related hypotheses of a connection between the Reynolds shear stress and the local mean velocity gradient. Mixing length theory with its concept of momentum transfer by fairly well organized lumps of fluid is considered a good first approximation to the behavior of turbulence dominated by large eddies. The large eddies carry most of the shear stress and their lifetime is so long that during it they may travel downstream for a considerable distance. Thus the Reynolds stress at a given position depends significantly on upstream history and is not, for example, uniquely determined by the local mean velocity gradient as in a laminar flow. This illustrates the need for transport equations to describe turbulence. The main reason for the success of mixing-length and eddy-viscosity is that many fluid flows used as test cases for turbulence models are nearly in a state of self-preservation or local equilibrium where profiles of mean velocity, Reynolds stresses, etc. are geometrically similar. Under such conditions both models work well. Complex flows, far from equilibrium, fare less well. In particular, for the airfoil boundary layer under consideration, mixing-length and eddy-viscosity models fail to predict levels of τ_{max} and cannot handle the outer part of the boundary layer where curvature effects appear to dominate. Clearly, more sophisticated turbulence models are required in order to predict such a complex flow.

REFERENCES

1. Schubauer, G.B. and Klebanoff, P.S., "Investigation of Separation of the Turbulent Boundary Layer," NACA Report 1030, 1951

2. Bidwell, J.M., "Application of the von Karman Momentum Theorem to Turbulent Boundary Layers," NACA TN 2571, 1951

3. Wadcock, A.J., "Flying-hot-wire Study of Two-dimensional Turbulent Separation on a NACA 4412 Airfoil at Maximum Lift," Ph.D. Thesis, California Institute of Technology, 1978

4. Coles, D. and Wadcock, A.J., "Flying-hot-wire Study of Two-dimensional Mean Flow Past a NACA 4412 Airfoil at Maximum Lift," AIAA Journal, Vol. 17, No. 4, April 1979

5. Wadcock, A.J., "Structure of the Turbulent Separated Flow Around a Stalled Airfoil," NASA CR 152263, 1979

6. So, R.M.C. and Mellor, G.L., "Experiment on Convex Curvature Effects in Turbulent Boundary Layers," J.F.M., Vol. 60, pp 43-62, 1973

7. Liepmann, H.W., "The Rise and Fall of Ideas in Turbulence," American Scientist, 1979

8. Galbraith, R.A.McD. and Head, M.R., "Eddy Viscosity and Mixing Length from Measured Boundary Layer Developments," Aero. Quarterly, Vol. XXVI, pp 133-154, 1975

9. Coles, D.E. and Hurst, E.A. (Editors), Proceedings of the Stanford Conference on Turbulent Boundary Layer Prediction, University Press, Stanford, California, 1968

10. Bradshaw, P., "Effects of Streamline Curvature on Turbulent Flow," AGARDograph No. 169, 1973.

TABLE 1

BOUNDARY LAYER INTEGRAL PARAMETERS

Station	x/c	$100\ \delta^*/c$	$100\ \Theta/c$	H	U_e/U_{ref}	R_Θ
50	0.620	0.827	0.393	2.10	1.295	7750
55	0.675	1.093	0.479	2.28	1.247	9110
60	0.731	1.526	0.600	2.54	1.207	11040
65	0.786	2.230	0.756	2.95	1.178	13560
70	0.842	3.288	0.913	3.60	1.158	16110
75	0.897	4.536	0.994	4.56	1.134	17170
80	0.953	5.845	1.014	5.76	1.112	17180

$c = 0.9012$ m

$U_{ref} = 27.13$ m/s

$\nu = 0.1605 \times 10^{-4}$ m^2/s

$R_\Theta = U_e \Theta / \nu$

TABLE 2

TURBULENCE CONTRIBUTIONS TO THE MOMENTUM INTEGRAL EQUATION

Station	x/c	A	B	C
55	0.675	-0.004	0.000	0.001
60	0.731	-0.006	0.000	0.001
65	0.786	-0.013	-0.001	0.003
70	0.842	-0.015	0.001	0.001
75	0.897	-0.012	0.001	0.002
80	0.953	-0.011	-0.003	0.006

A: $\quad -\dfrac{1}{U_e^2} \displaystyle\int_0^\delta \dfrac{\partial}{\partial x} (\overline{u'u'})\, dy$

B: $\quad -\dfrac{\delta}{U_e^2} \displaystyle\int_0^\delta \dfrac{\partial^2}{\partial x^2} (\overline{u'v'})\, dy$

C: $\quad \dfrac{1}{U_e^2} \displaystyle\int_0^\delta \int_0^y \dfrac{\partial}{\partial x} \left(\dfrac{\partial}{\partial x} (\overline{u'v'}) + \dfrac{\partial}{\partial y} (\overline{v'v'}) \right) dy\, dy$

STATION
50

y, v

BOUNDARY LAYER
COORDINATES

x, u

y, v

x, u

α = 13.87°

IX = 50
x/c = 0.620

NACA 4412 AIRFOIL SECTION
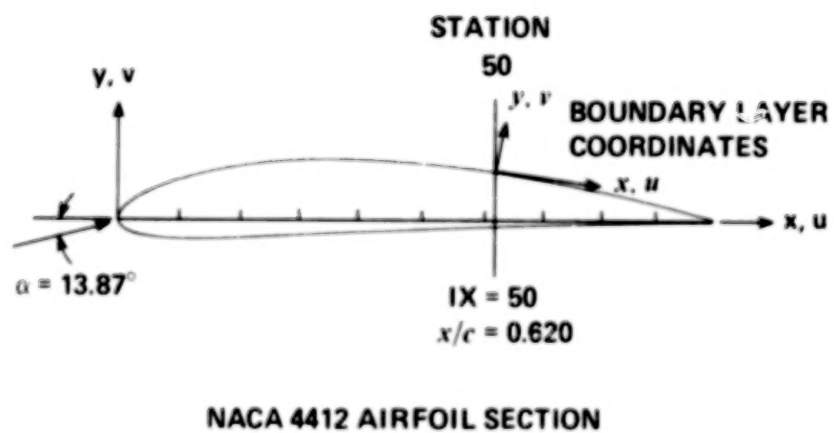
Figure 1.   Airfoil geometry and orientation of axes.
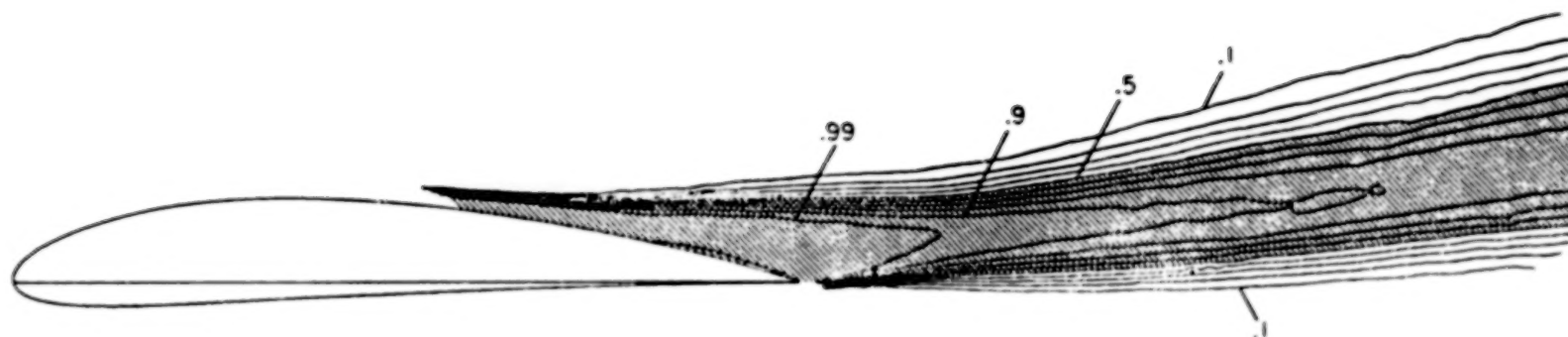
Figure 2. Contour plot of intermittency factor from final processed data. Contour interval 0.1.
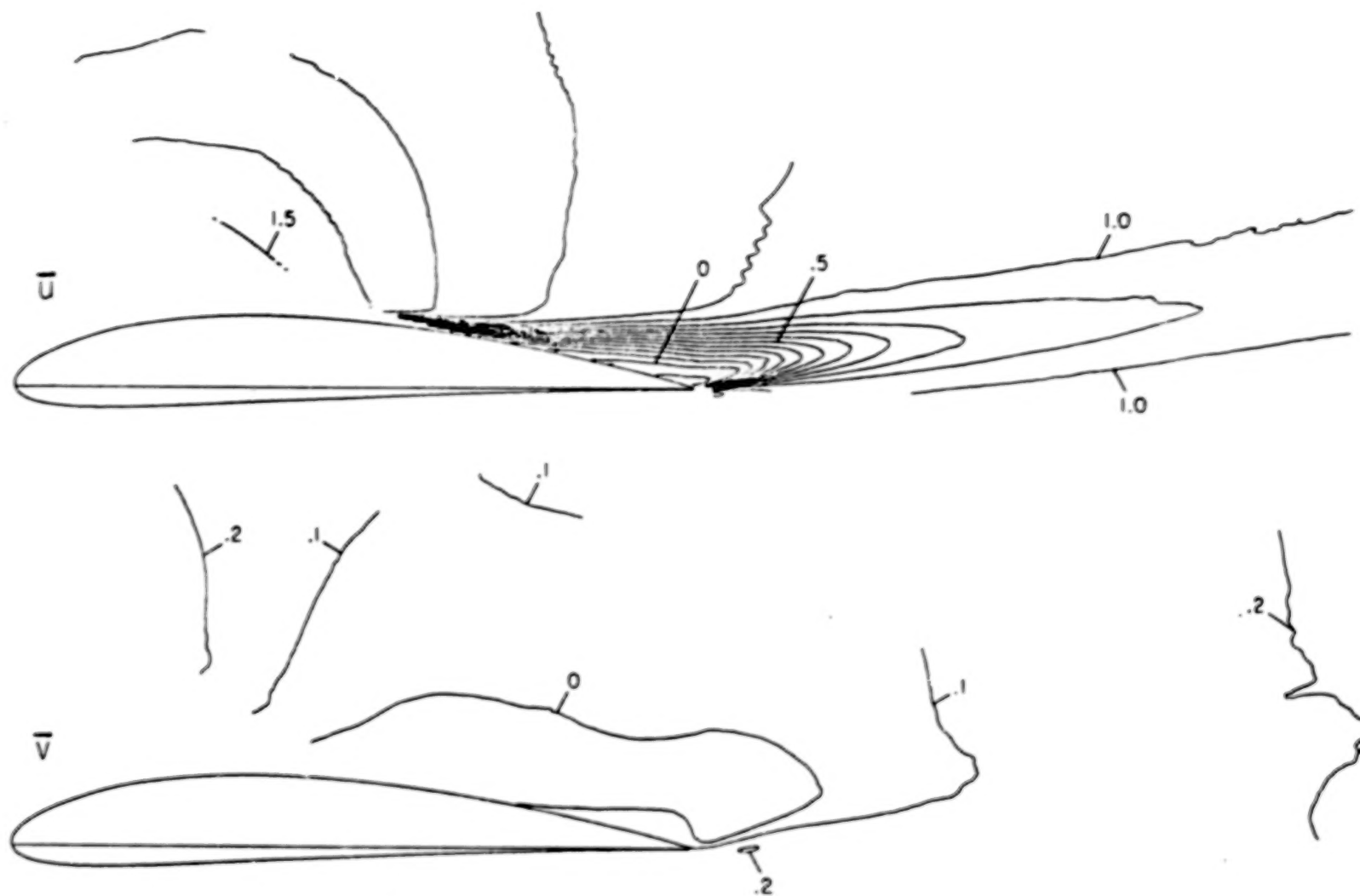
Figure 3.   Contour plots of dimensionless mean-velocity components $\bar{u}/U_{REF}$, $\bar{v}/U_{REF}$ from final processed data.   Contour interval 0.1.

33
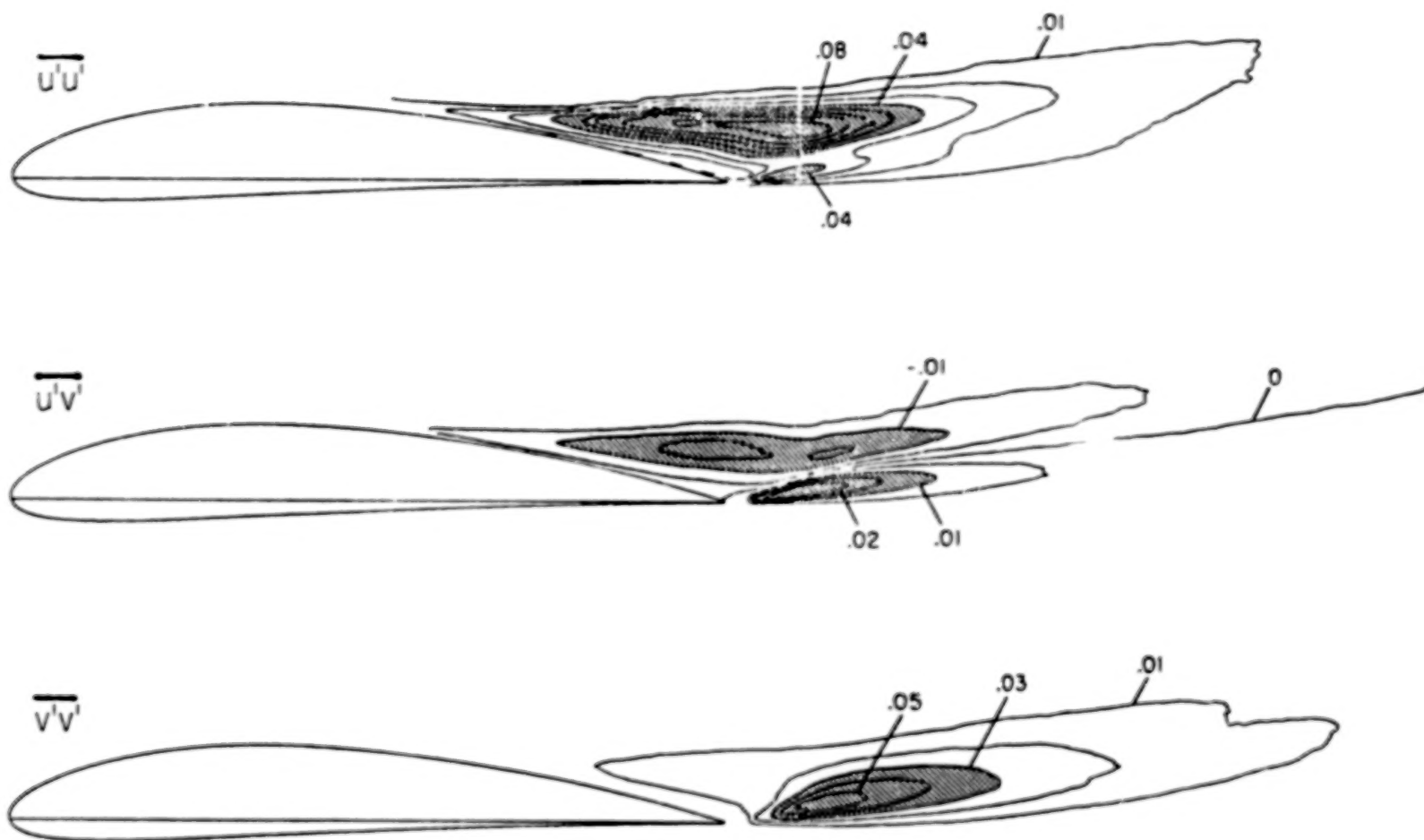
Figure 4. Contour plots of dimensionless double correlations from final
processed data. Contour intervals: $\overline{u'u'}/U^2_{REF}$; 0.010

$\overline{u'v'}/U^2_{REF}$; 0.005

$\overline{v'v'}/U^2_{REF}$; 0.010
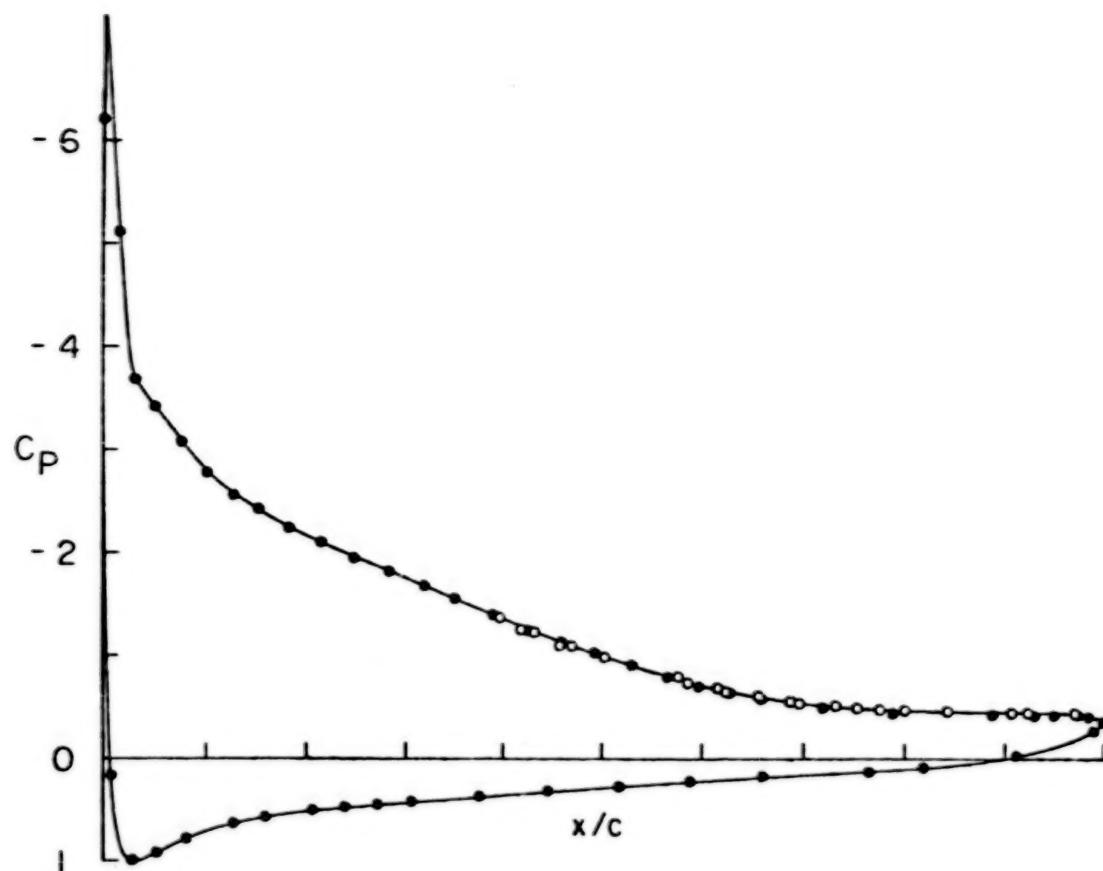
Figure 5. Surface-pressure distribution at nominal 14 degrees angle of incidence.
Solid symbols: data at midspan. Open symbols: data at 1/4- and 3/4-span.

35

FLOW GUIDE

TURBULENCE
AT MIDSPAN

(a)

H/Q_ref

.8   1.0

RUN
30

60

Y, cm

50

20

10
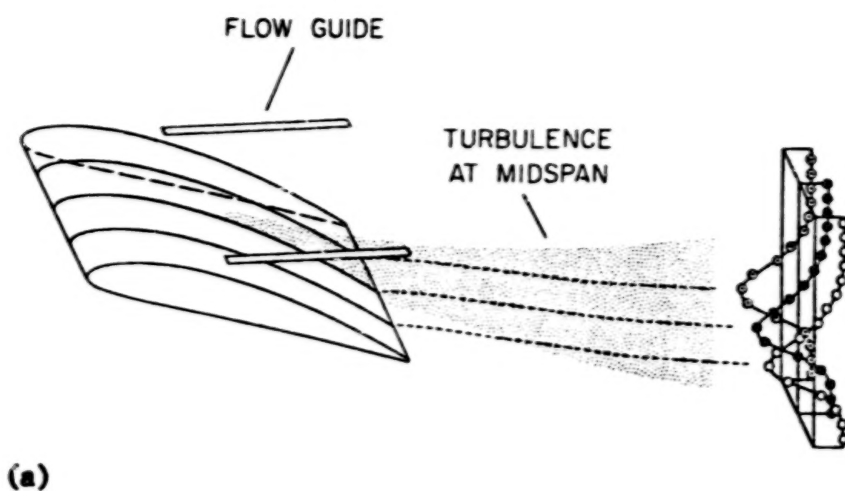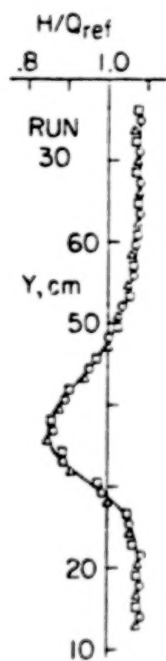
(b)

Figure 6. (a) Configuration of model and wake.
                View is inverted from actual
                orientation in tunnel.

            (b) Two-dimensionality of wake with
                flow guides in optimum position.
                H is total pressure in wake referred
                to atmospheric pressure.
                Measurement position is 1.28 chords
                downstream of airfoil trailing edge.
                Airfoil is lifting in direction of
                increasing Y.
                △   South
                ○   Center
                □   North

36
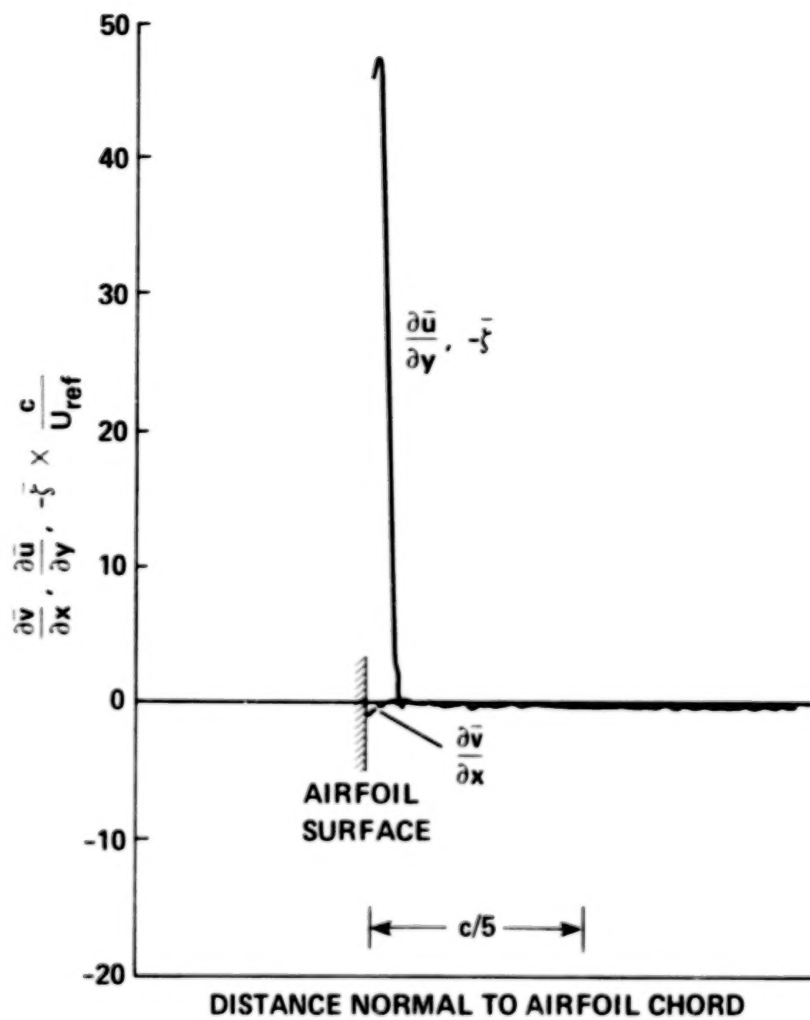
Figure 7.   Vorticity distribution at IX = 5C, x/c = 0.620; $\bar{\xi} = \dfrac{\partial \bar{v}}{\partial x} - \dfrac{\partial \bar{u}}{\partial y}$.
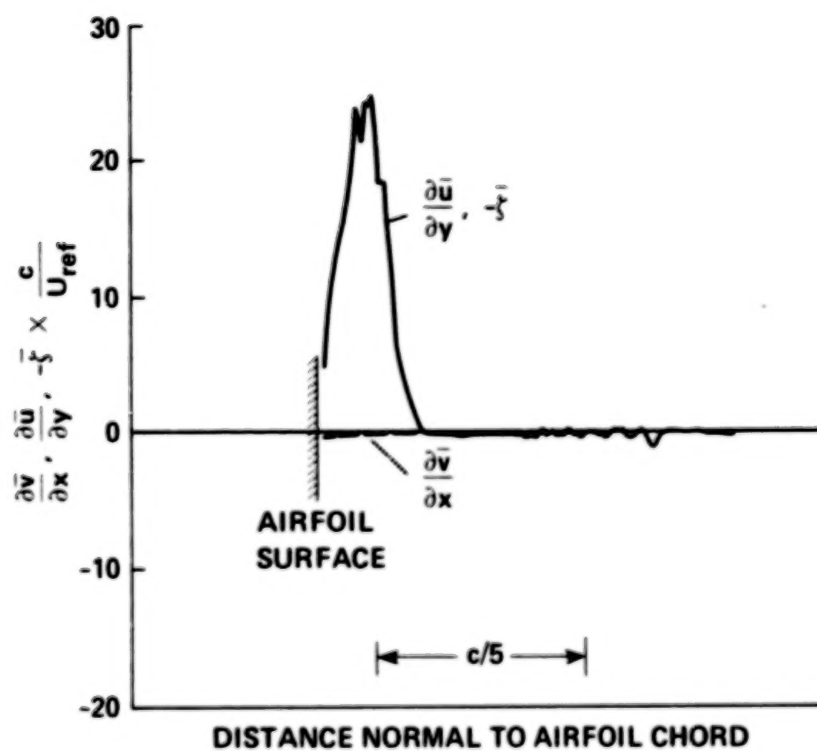
Figure 8. Vorticity distribution at IX = 75, x/c = 0.897; $\bar{\xi} = \dfrac{\partial \bar{v}}{\partial x} - \dfrac{\partial \bar{u}}{\partial y}$.
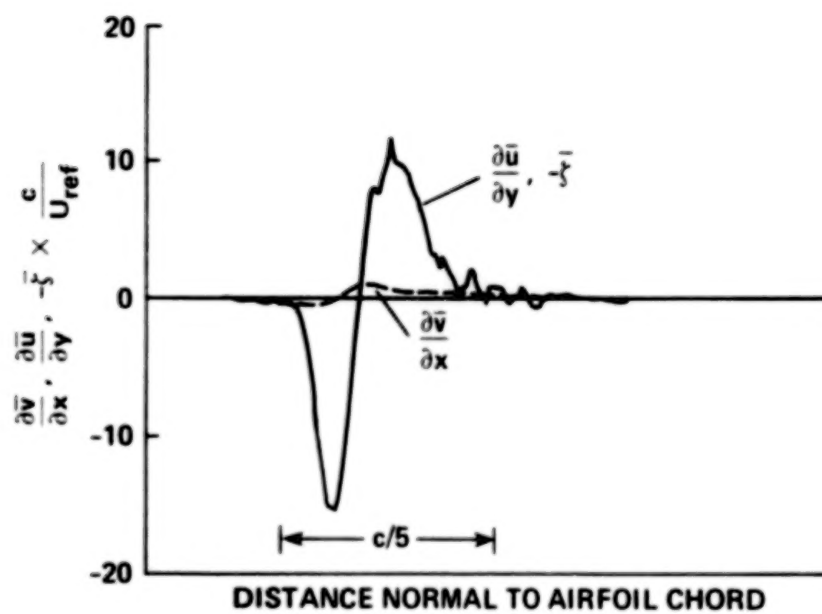
Figure 9. Vorticity distribution at IX = 100, x/c = 1.175; $\bar{\xi} = \dfrac{\partial \bar{v}}{\partial x} - \dfrac{\partial \bar{u}}{\partial y}$.
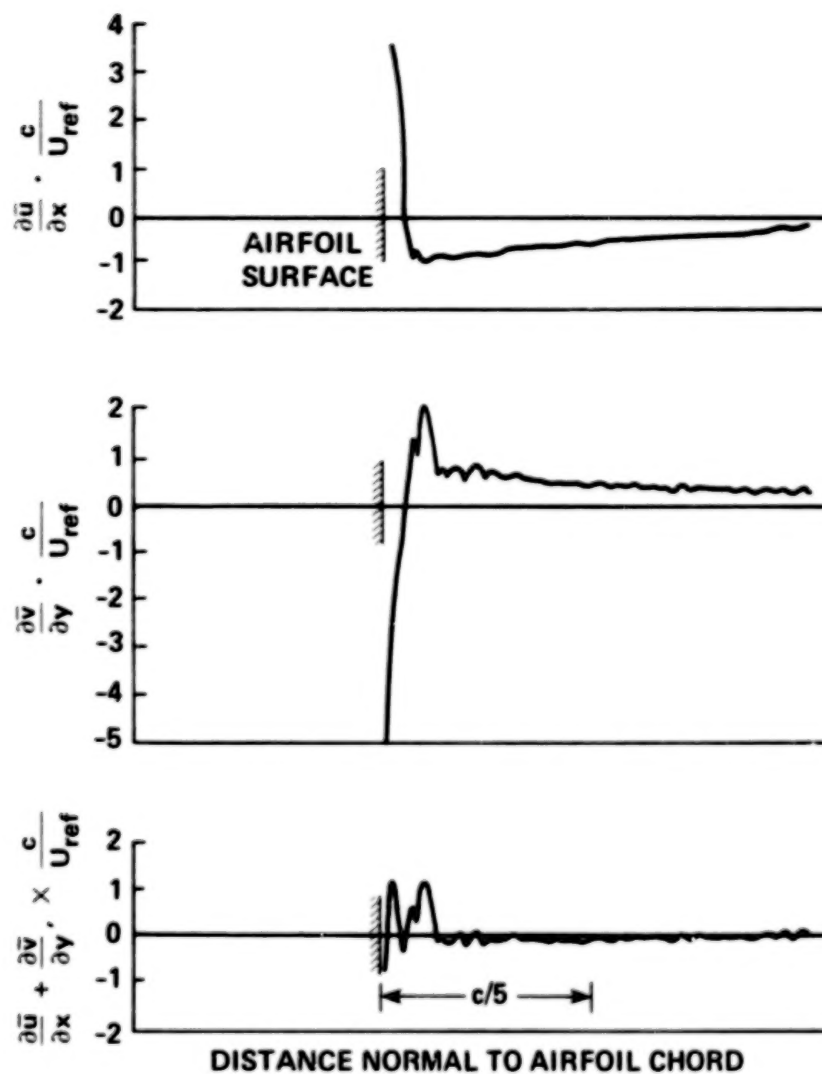
Figure 10. Conservation of mass at IX = 50, x/c = 0.620; $\frac{\partial \bar{u}}{\partial x} + \frac{\partial \bar{v}}{\partial y} = -\frac{\partial \bar{w}}{\partial z}$.

40
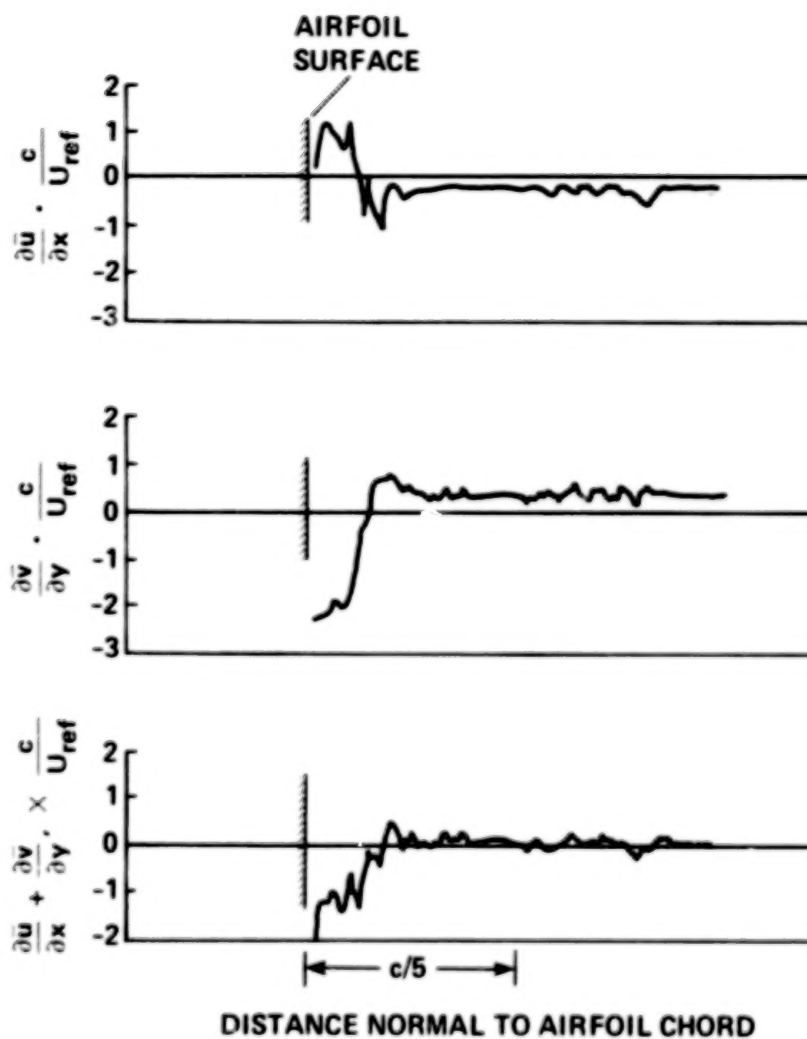
Figure 11. Conservation of mass at IX = 75, x/c = 0.897; $\frac{\partial \bar{u}}{\partial x} + \frac{\partial \bar{v}}{\partial y} = -\frac{\partial \bar{w}}{\partial z}$.

41
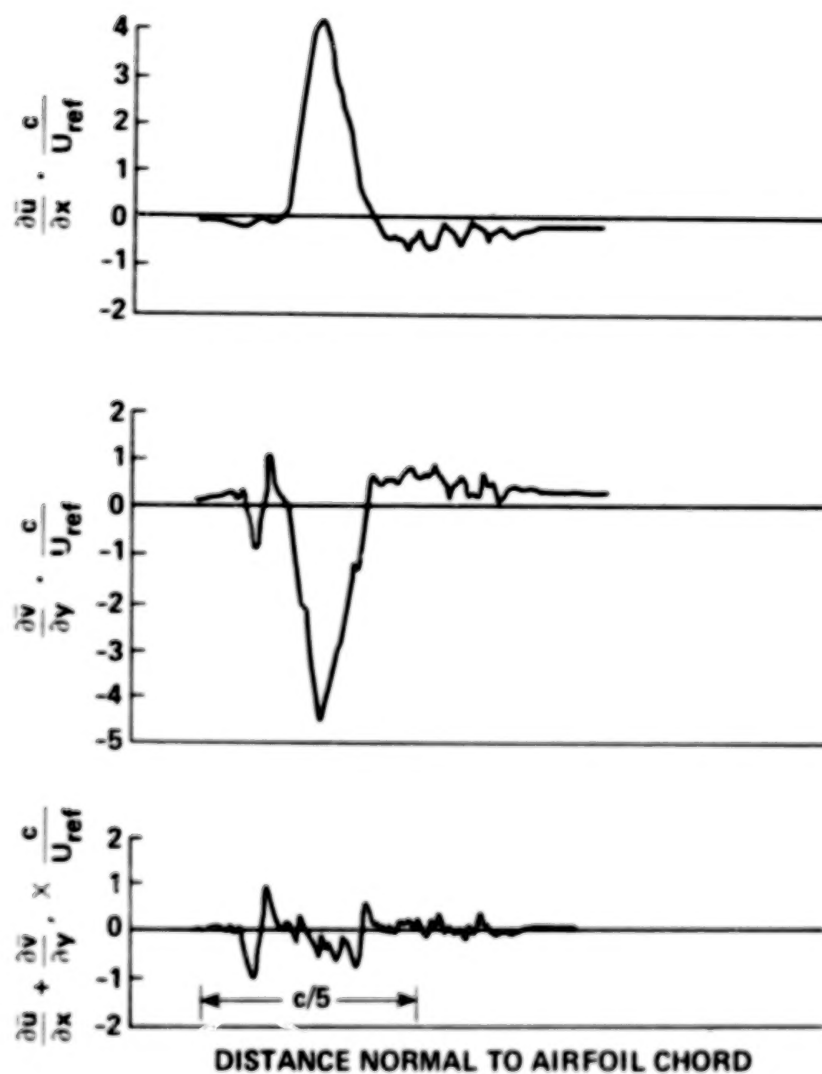
Figure 12. Conservation of mass at IX = 100, x/c = 1.175; $\frac{\partial \bar{u}}{\partial x} + \frac{\partial \bar{v}}{\partial y} = -\frac{\partial \bar{w}}{\partial z}$.
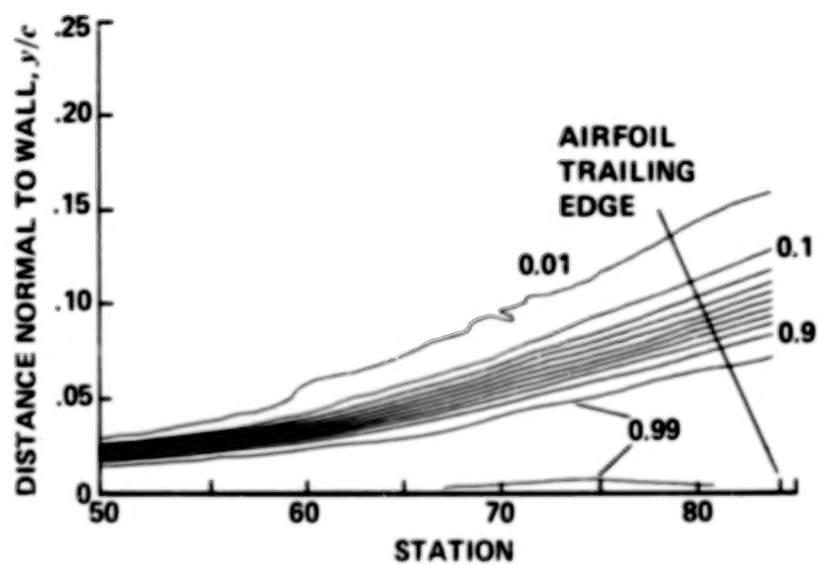
Figure 13. Contour plot of intermittency factor. Contour interval is 0.1.
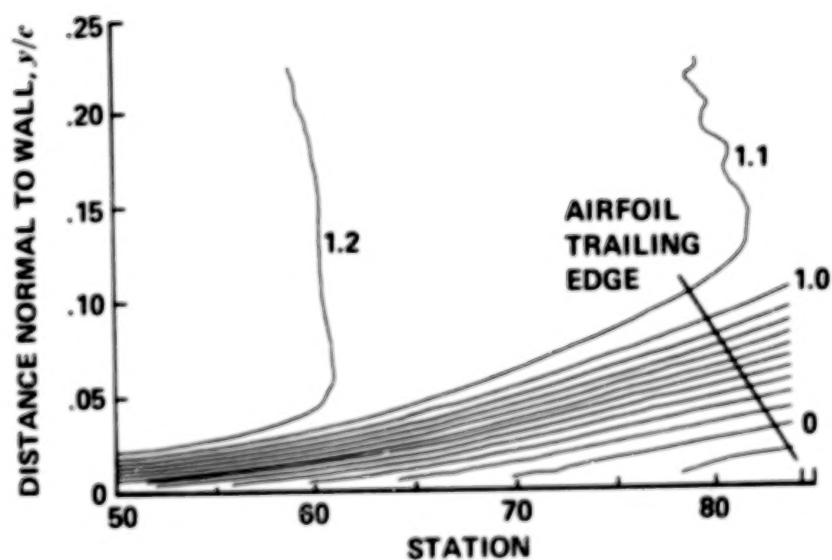
Figure 14. Contour plot of mean-velocity component parallel t) surface, U/U_{ref}. Contour interval 0.1.
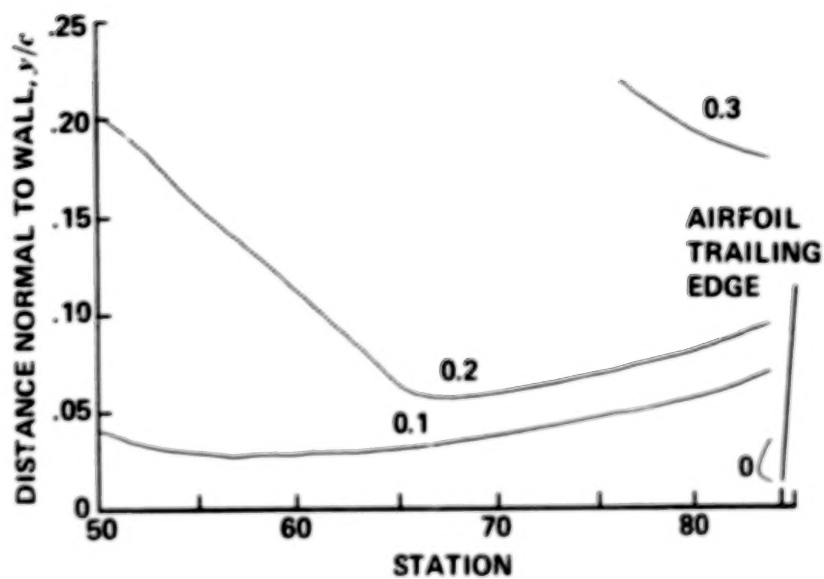
Figure 15. Contour plot of mean-velocity component normal to surface, V/U_{REF}. Contour interval 0.1.
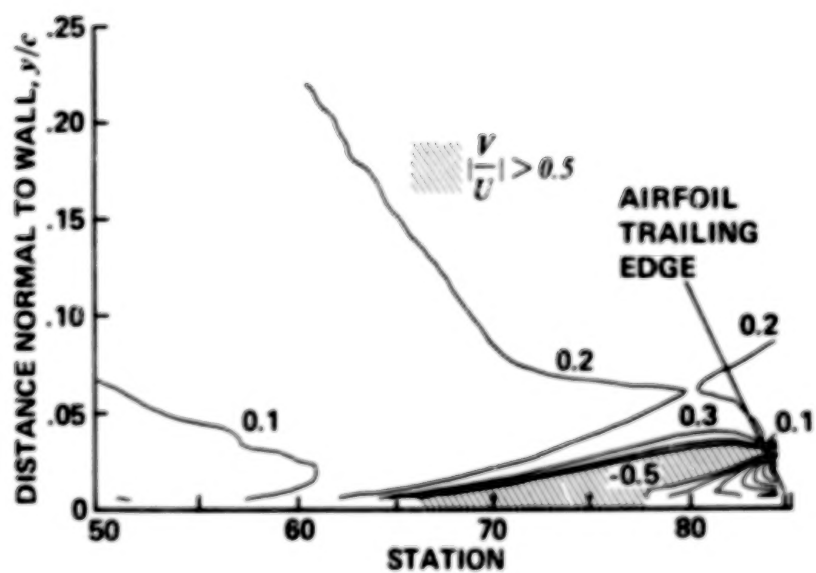
Figure 16. Contour plot of mean-velocity component ratio, V/U. Contour interval 0.1.
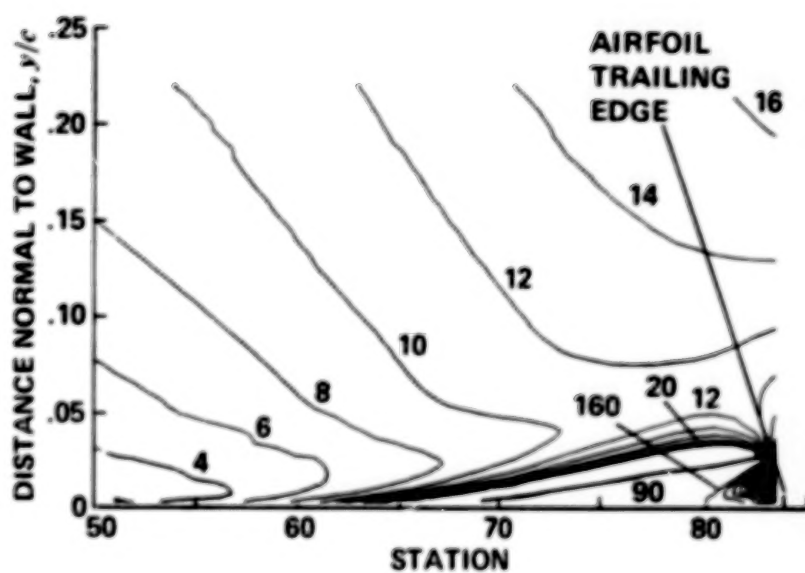
Figure 17. Contour plot of mean flow direction, $\alpha^\circ = \tan^{-1}(V/U)$. Contour interval 2 degrees.
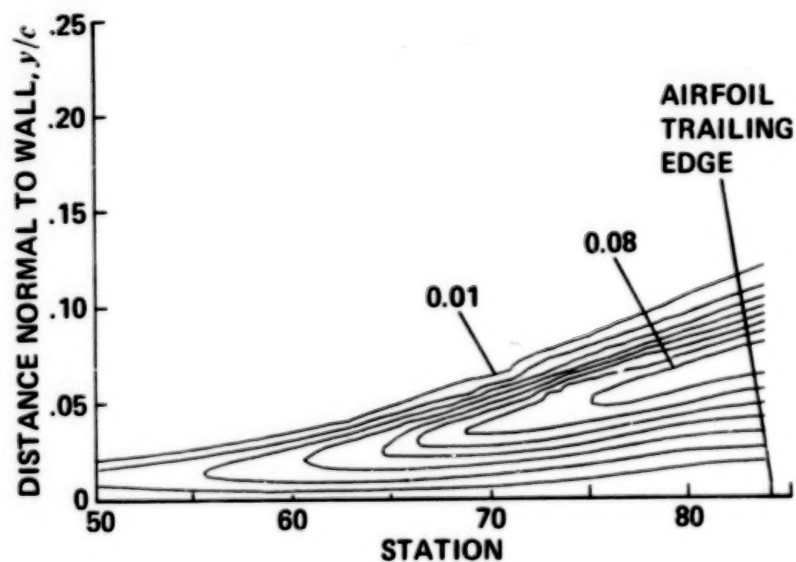
Figure 18. Contour plot of double correlation, $\overline{u'u'}/U_{REF}^2$.
Contour interval 0.01.
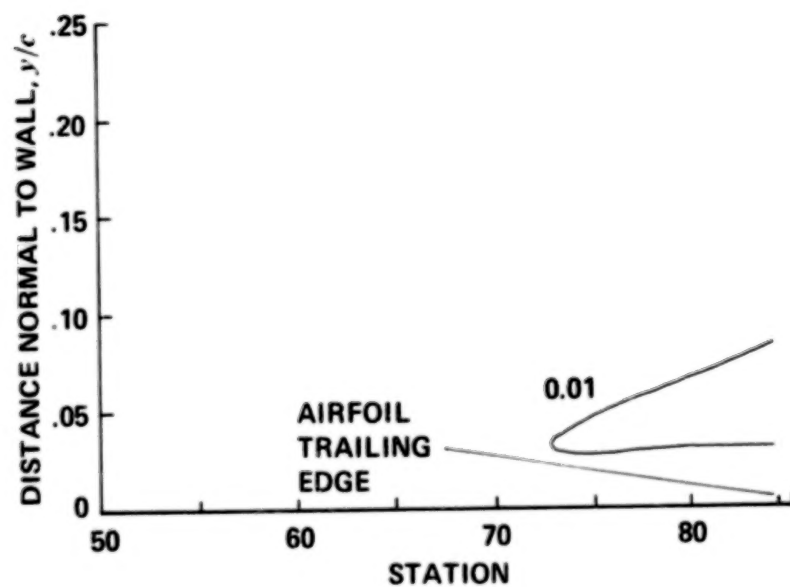
Figure 19. Contour plot of double correlation, $\overline{v'v'}/U_{REF}^2$. Contour interval 0.01.
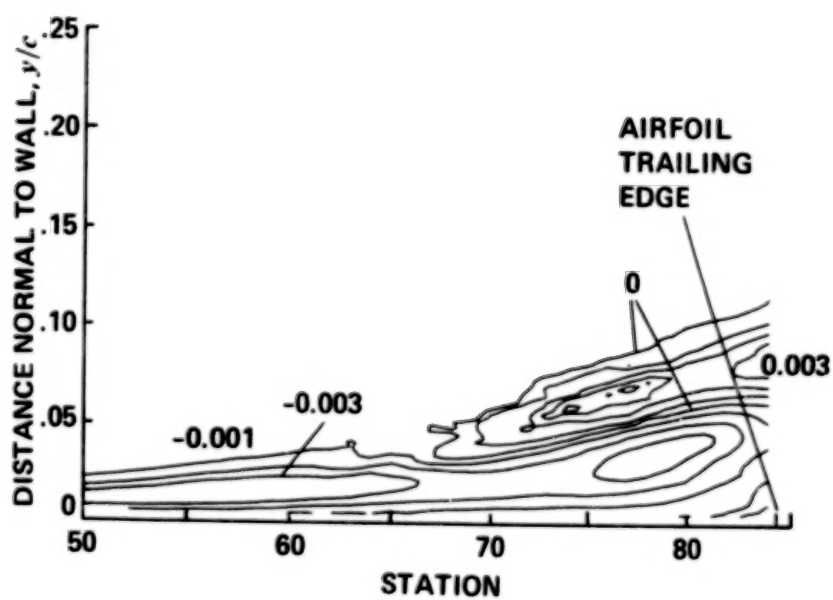
Figure 20.   Contour plot of double correlation, $\overline{u'v'}/U_{REF}^2$. Contour interval 0.001.
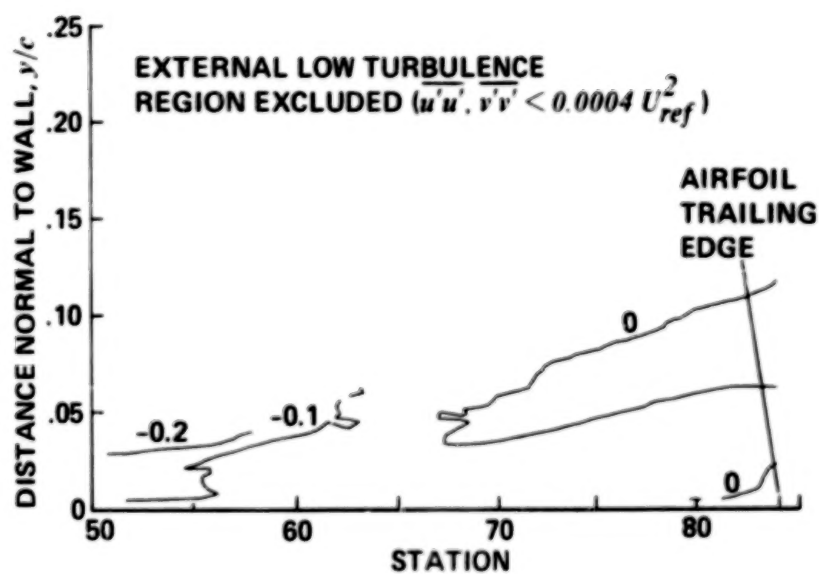
Figure 21.   Contour plot of correlation coefficient, $\overline{u'v'}/(\overline{u'u'} + \overline{v'v'})$. Contour interval 0.1.
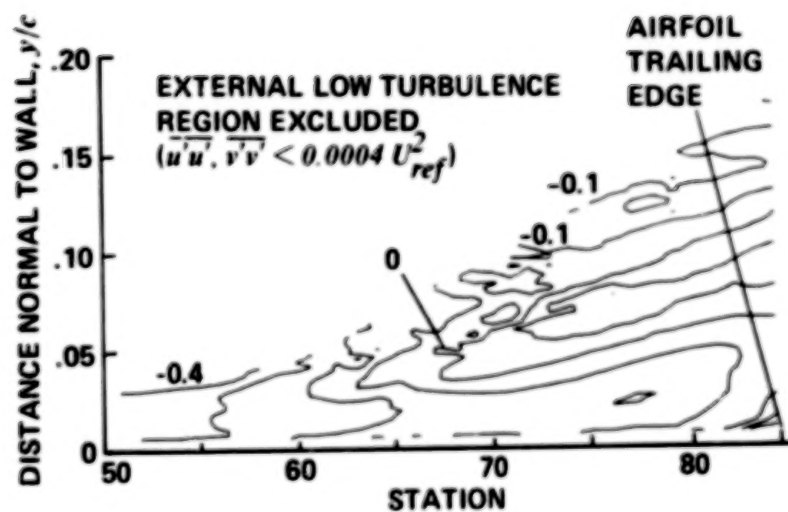
Figure 22. Contour plot of correlation coefficient, $\overline{u'v'}\big/(\overline{u'u'})^{\frac{1}{2}}(\overline{v'v'})^{\frac{1}{2}}$. Contour interval 0.1.
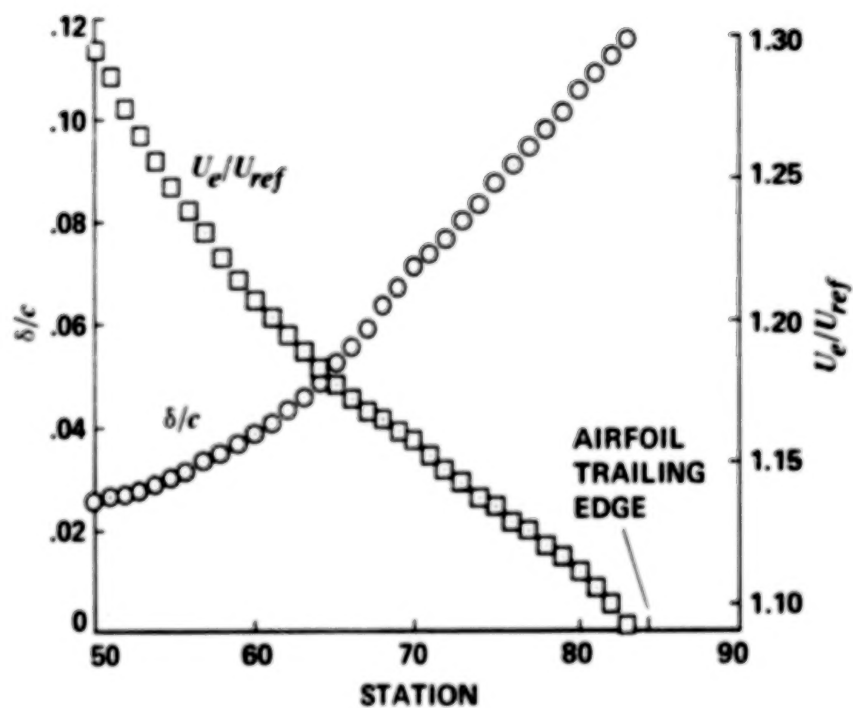
Figure 23.   Boundary layer thickness and external velocity as a
function of streamwise position.
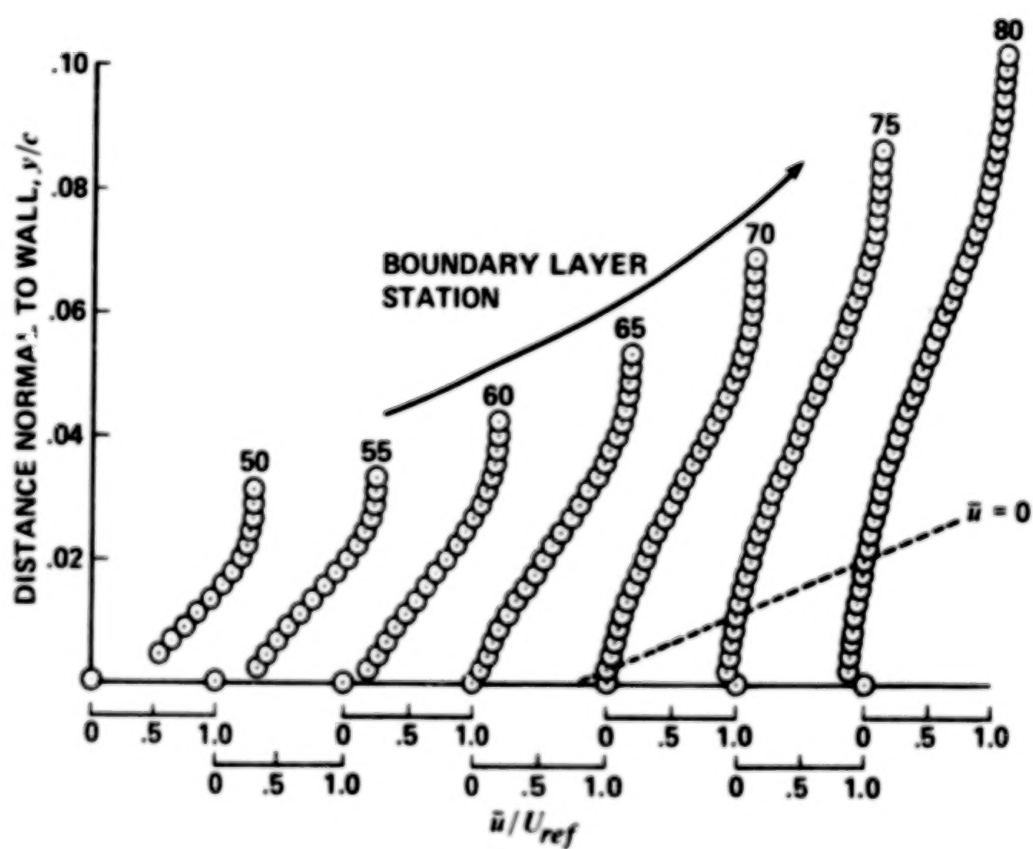
Figure 24. Boundary layer development as a function of streamwise position.
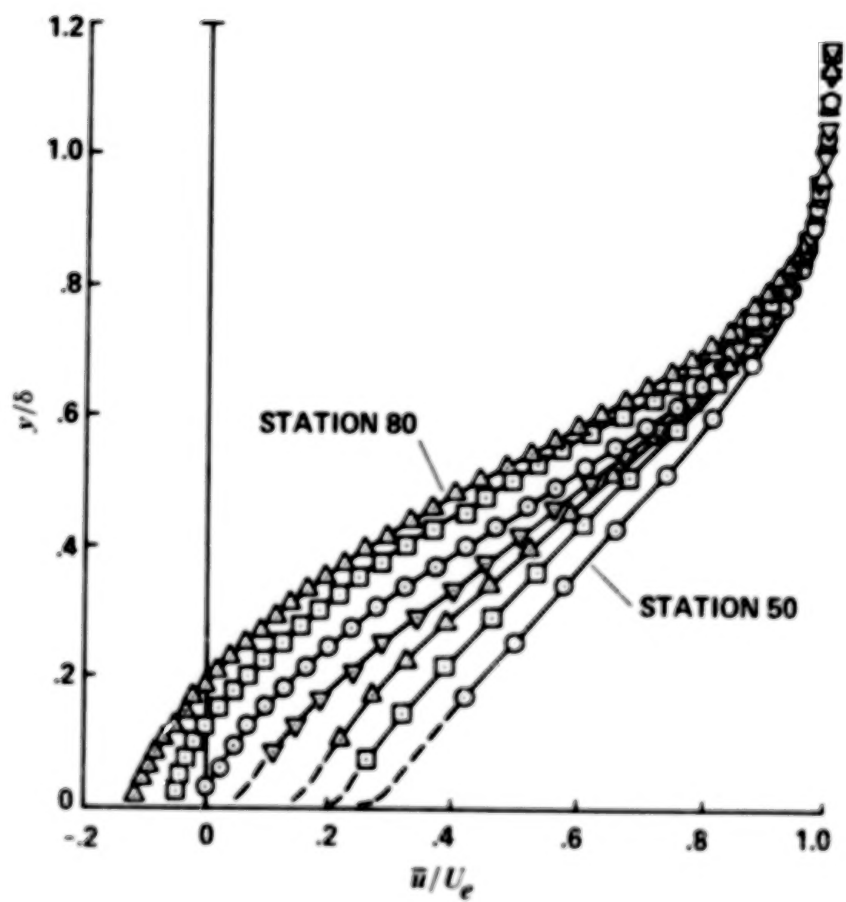
Figure 25. Non-dimensional boundary layer velocity profiles.
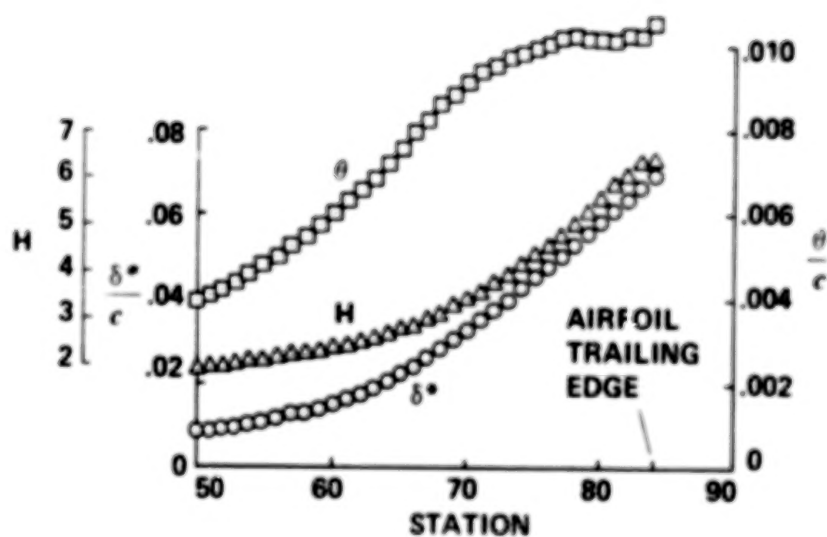
Figure 26. Variation of displacement thickness, momentum thickness and shape factor along airfoil surface.
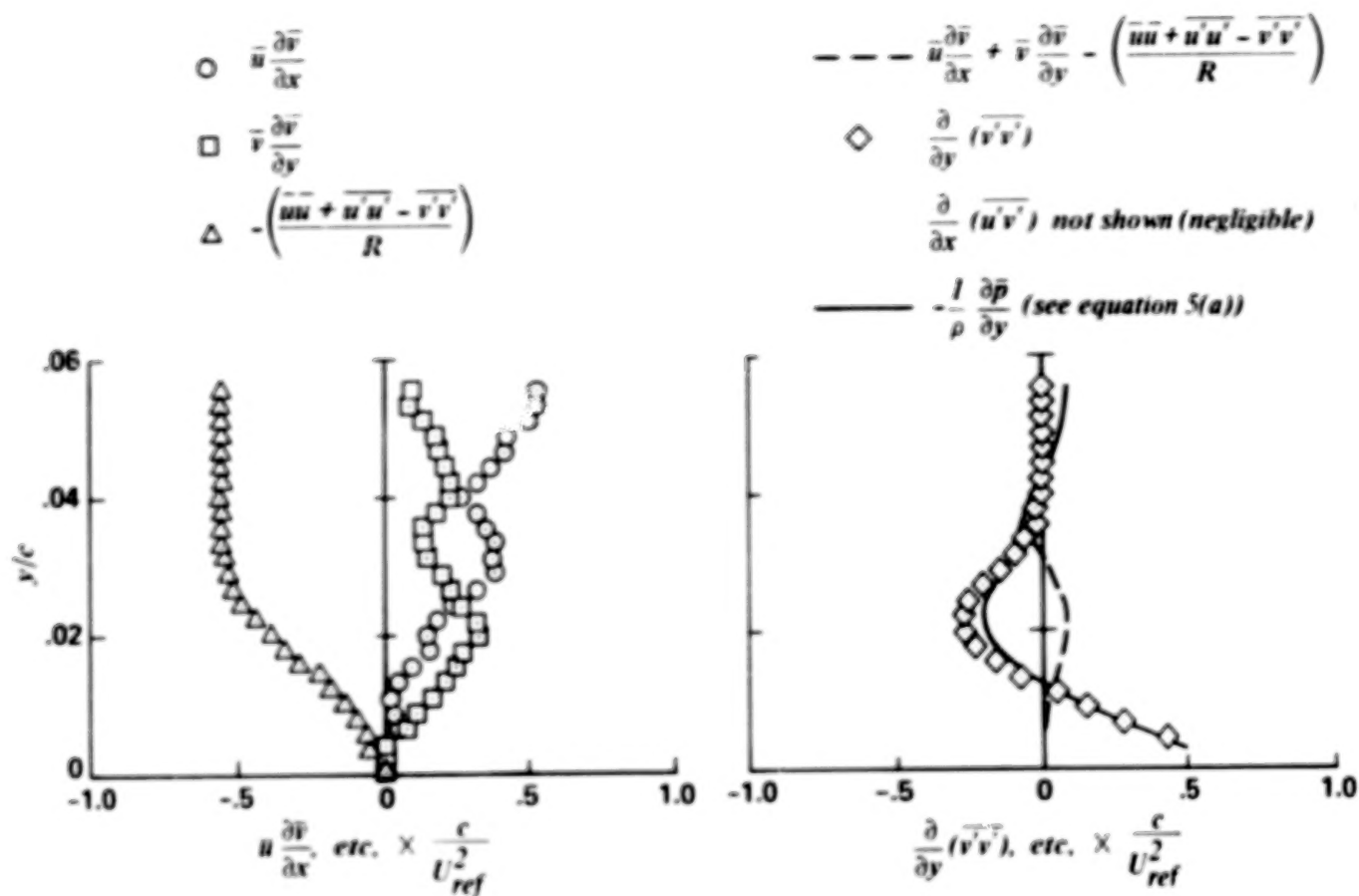
Figure 27. Examination of time-mean y-momentum equation at Station 55.

57
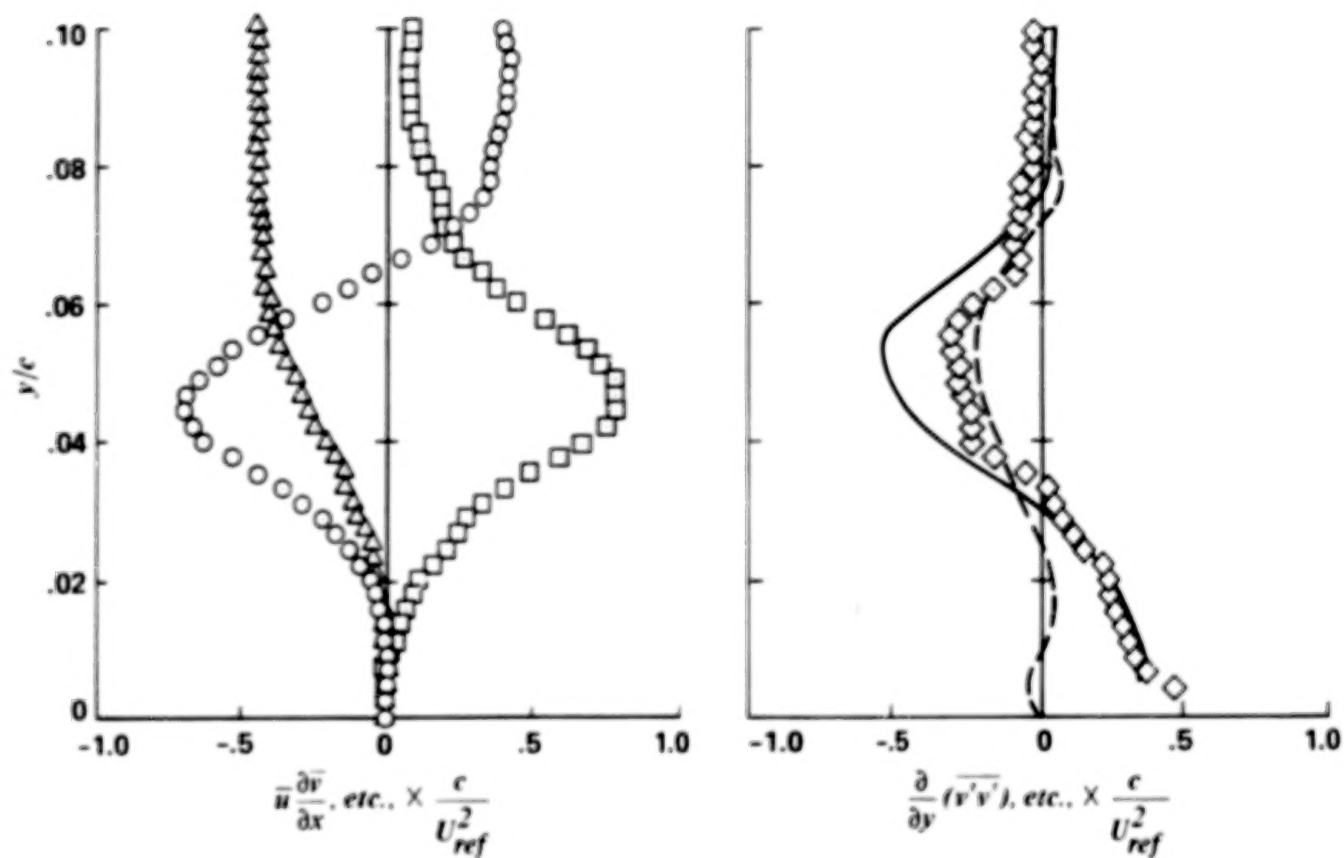
Figure 28. Examination of time-mean y-momentum equation at Station 70. See Figure 27 for legend.

BLANK PAGE

BLANK PAGE
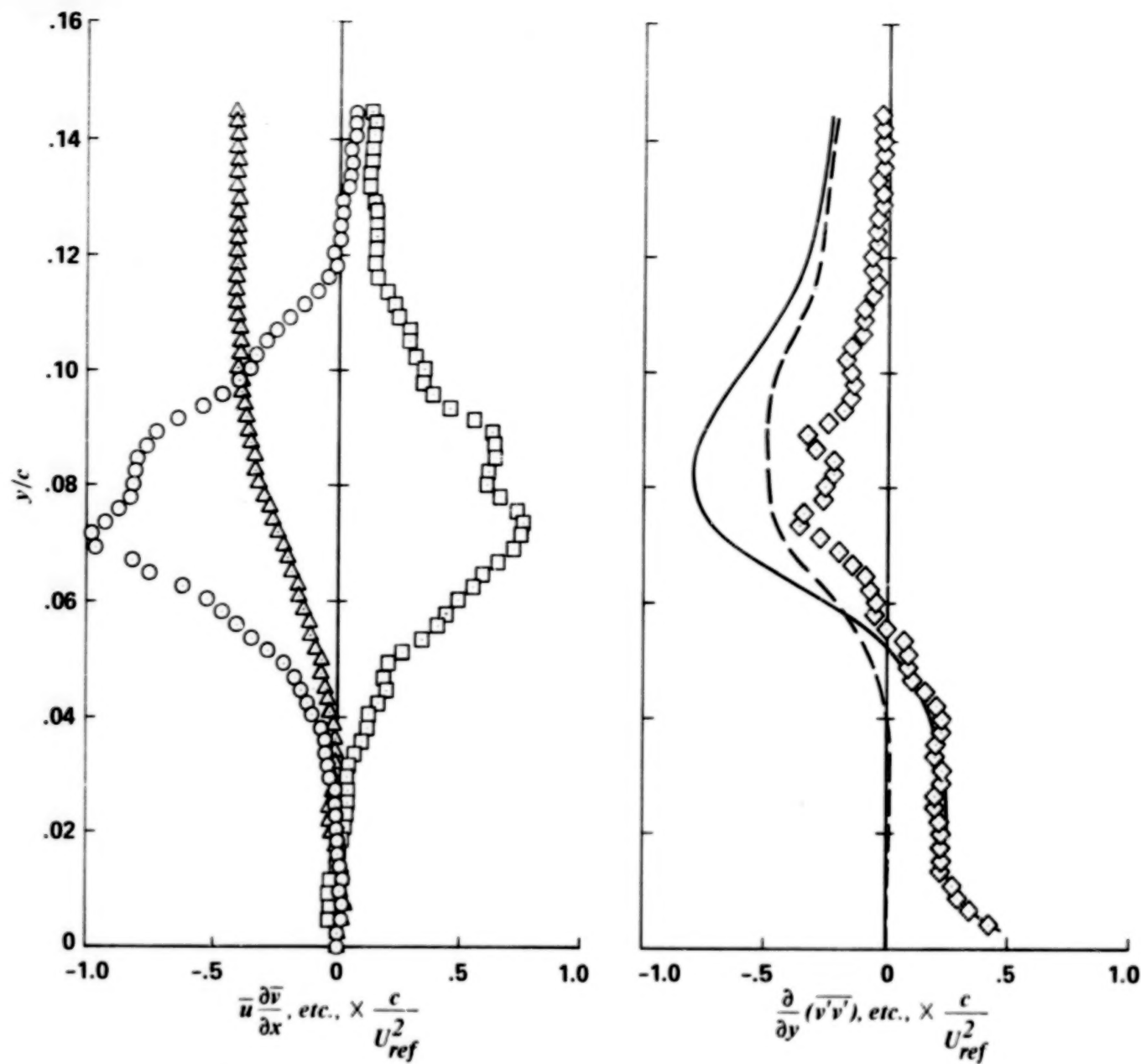
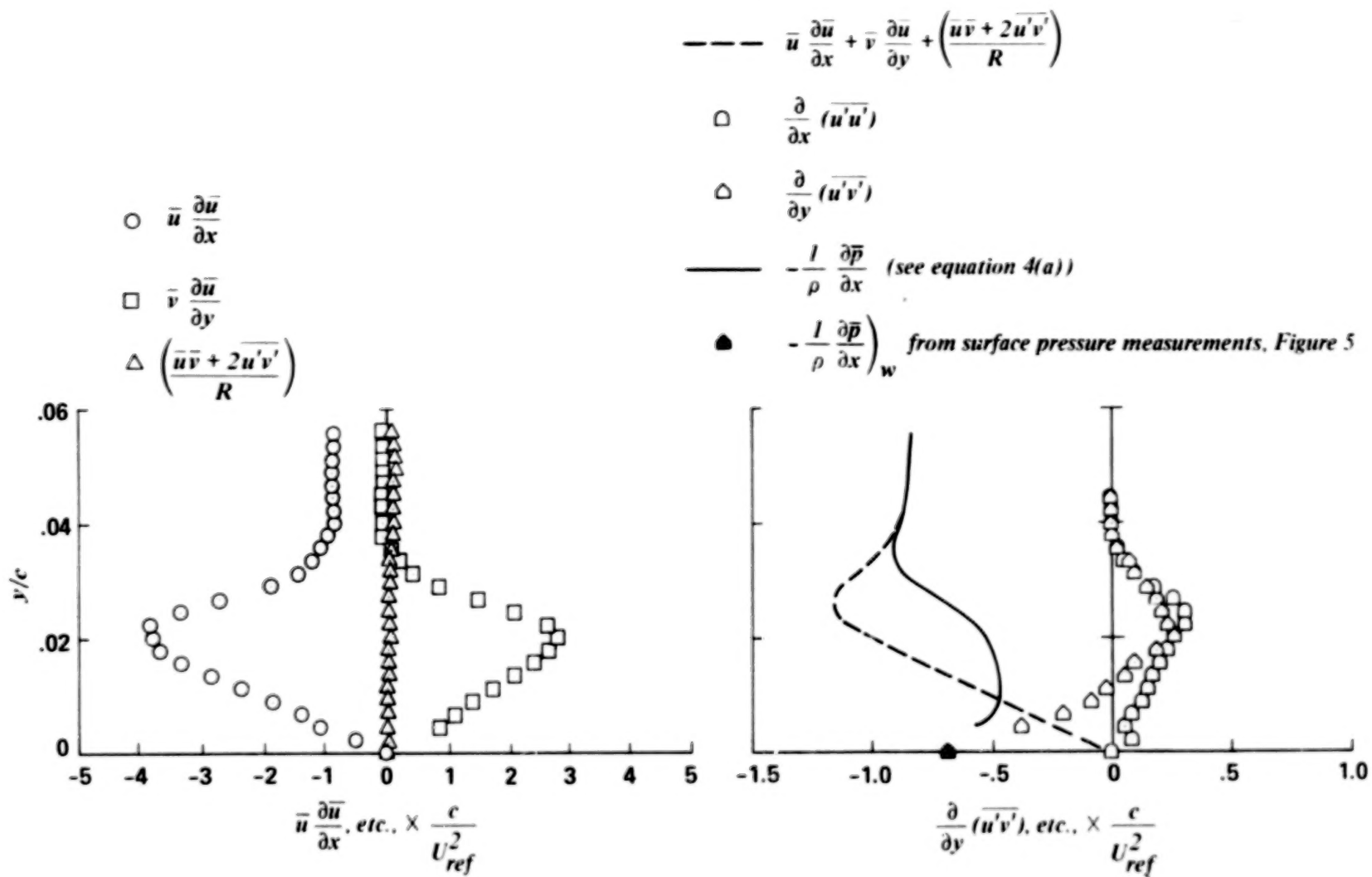Figure 29. Examination of time-mean y-momentum equation at Station 80. See Figure 27 for legend.

$$--- \quad \bar{u}\,\frac{\partial \bar{u}}{\partial x} + \bar{v}\,\frac{\partial \bar{u}}{\partial y} + \left(\frac{\bar{u}\bar{v} + 2\overline{u'v'}}{R}\right)$$

$\triangle \quad \dfrac{\partial}{\partial x}\,(\overline{u'u'})$

$\triangle \quad \dfrac{\partial}{\partial y}\,(\overline{u'v'})$

$$\underline{\qquad} \quad -\frac{1}{\rho}\,\frac{\partial \bar{p}}{\partial x} \quad \textit{(see equation 4(a))}$$

$\blacktriangle \quad -\dfrac{1}{\rho}\,\dfrac{\partial \bar{p}}{\partial x}\Big)_{w} \quad \textit{from surface pressure measurements, Figure 5}$

$\circ \quad \bar{u}\,\dfrac{\partial \bar{u}}{\partial x}$

$\square \quad \bar{v}\,\dfrac{\partial \bar{u}}{\partial y}$

$\triangle \quad \left(\dfrac{\bar{u}\bar{v} + 2\overline{u'v'}}{R}\right)$

Figure 30.   Examination of time-mean x-momentum equation at Station 55.
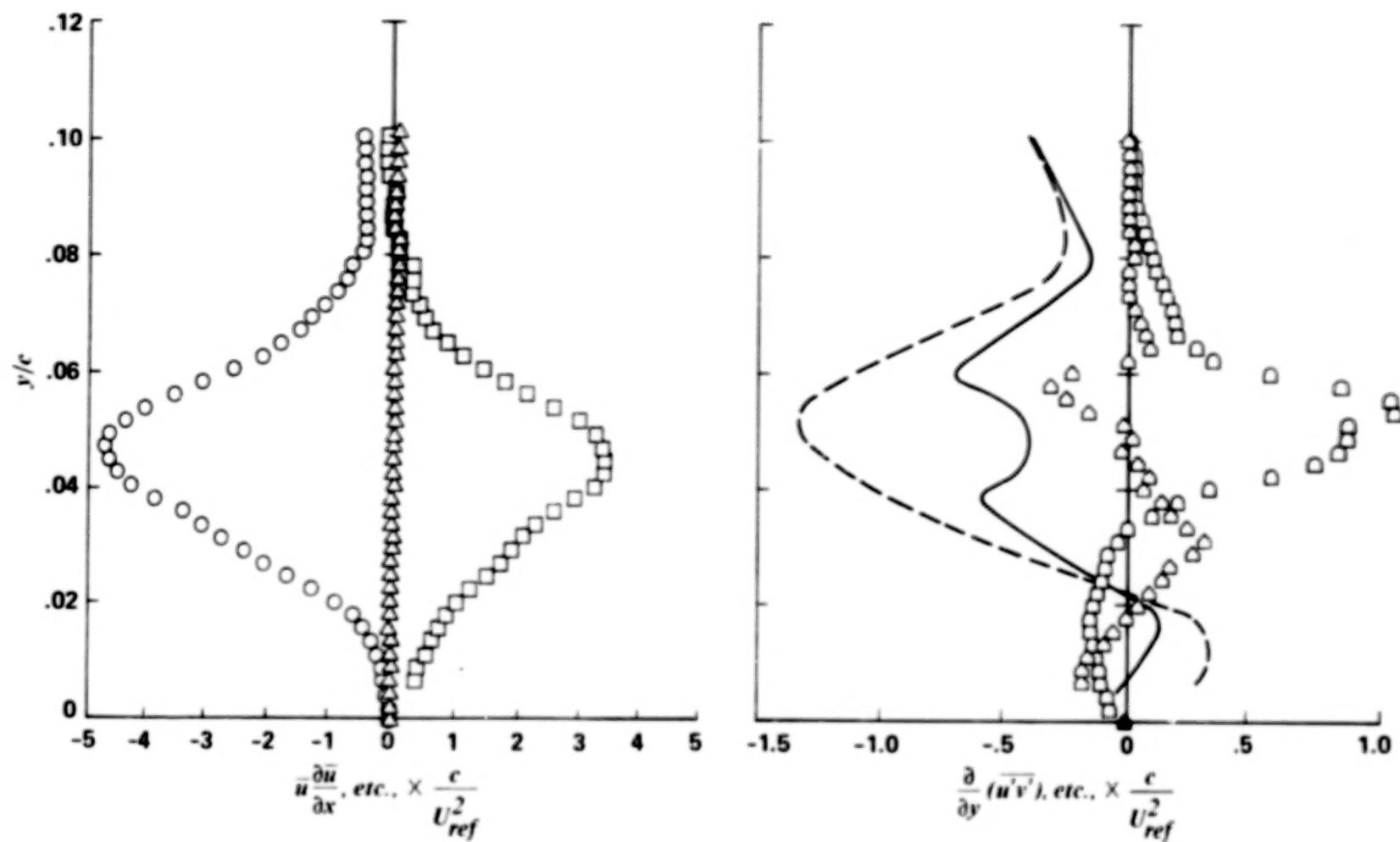
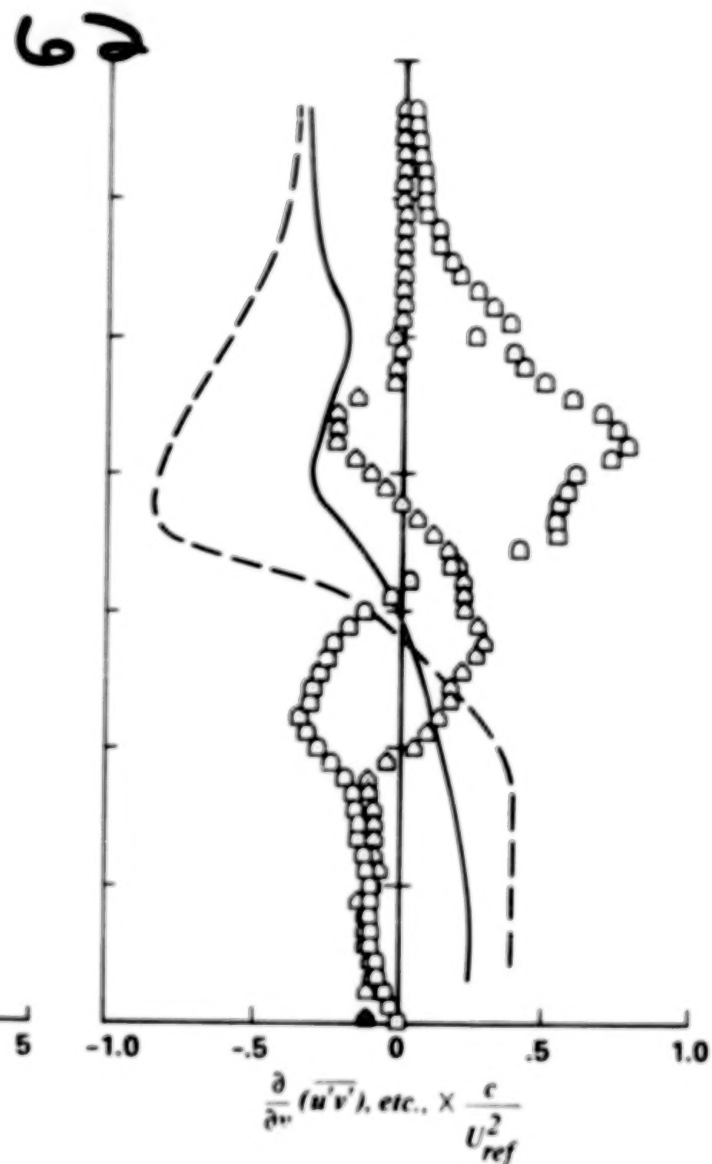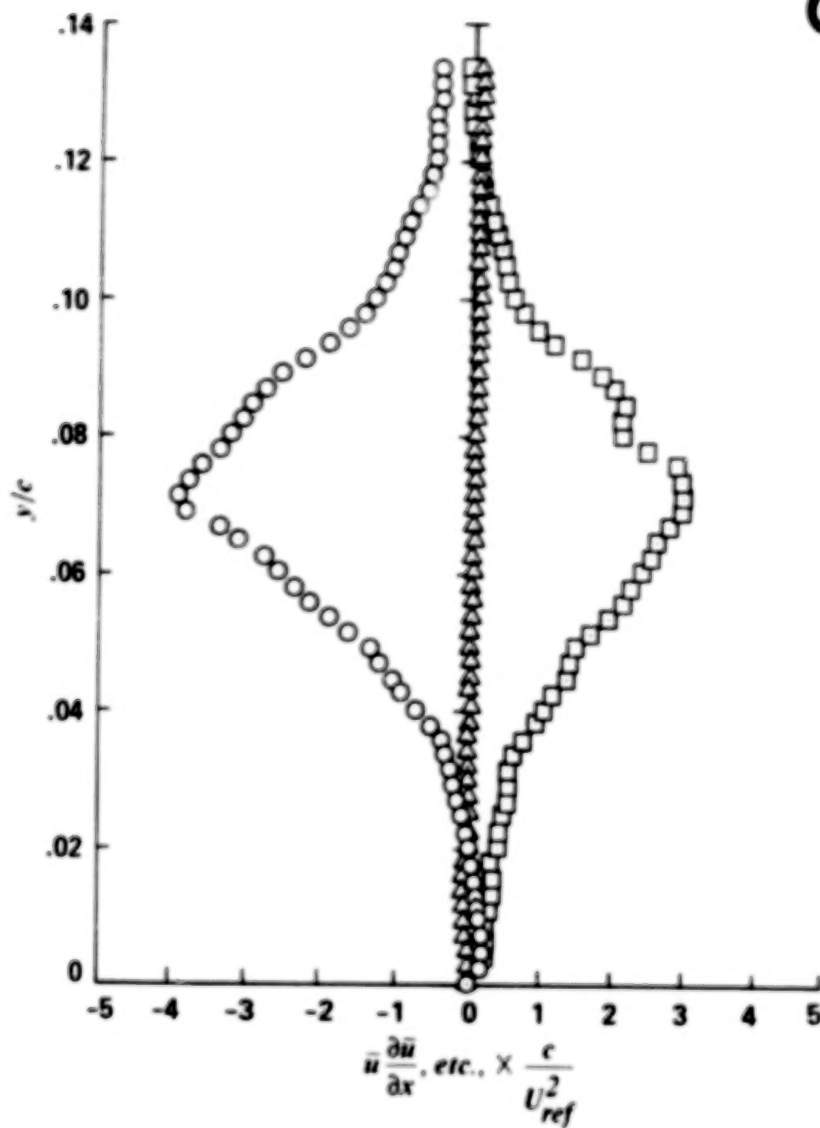Figure 31. Examination of time-mean x-momentum equation at Station 70. See Figure 30 for legend.

Figure 32. Examination of time-mean x-momentum equation
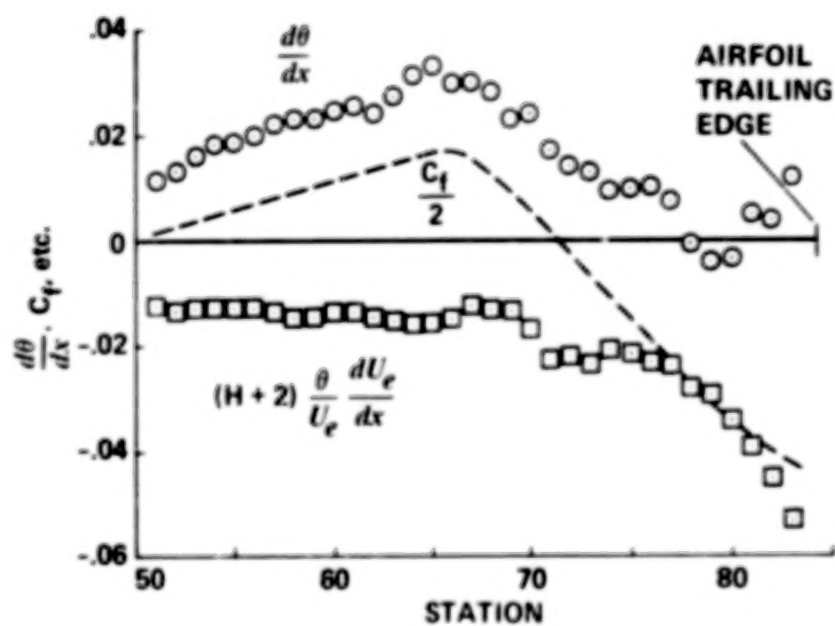at Station 80. See Figure 30 for legend.

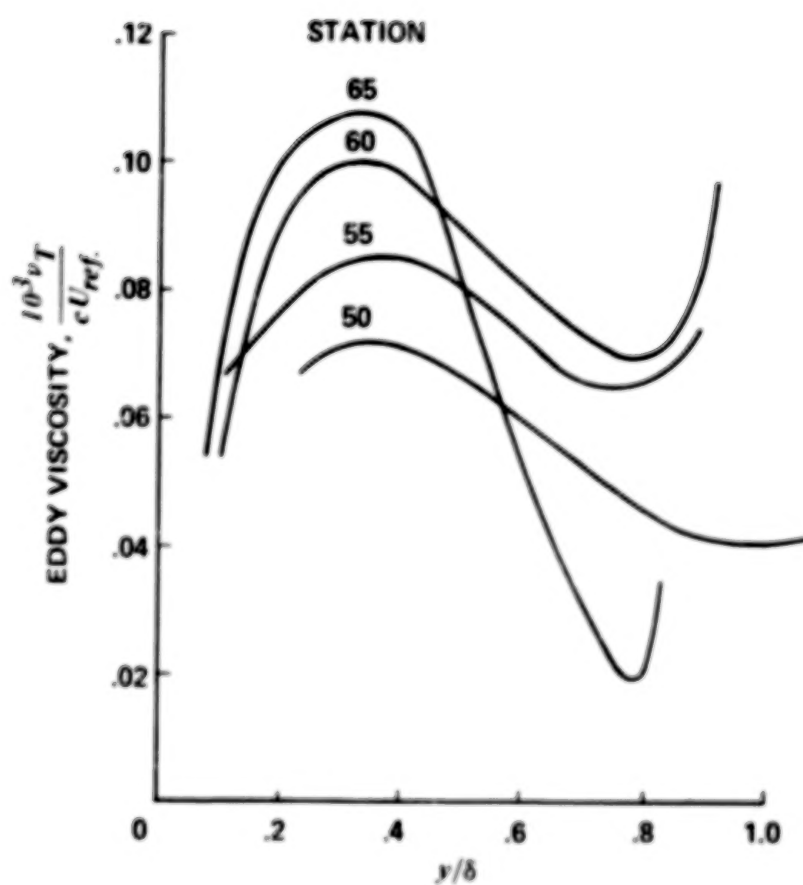Figure 33. Examination of momentum integral equation.

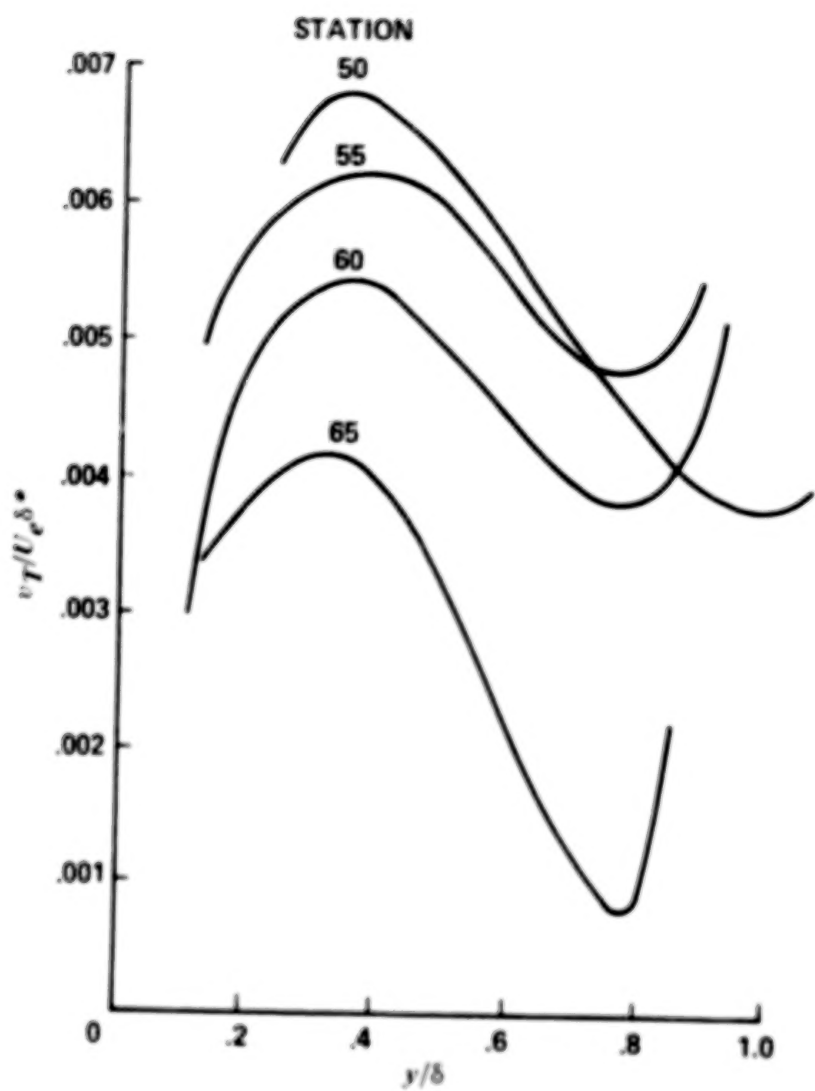Figure 34. Variation of eddy viscosity through attached boundary layer.

Figure 35.   Variation of eddy viscosity through attached boundary layer.
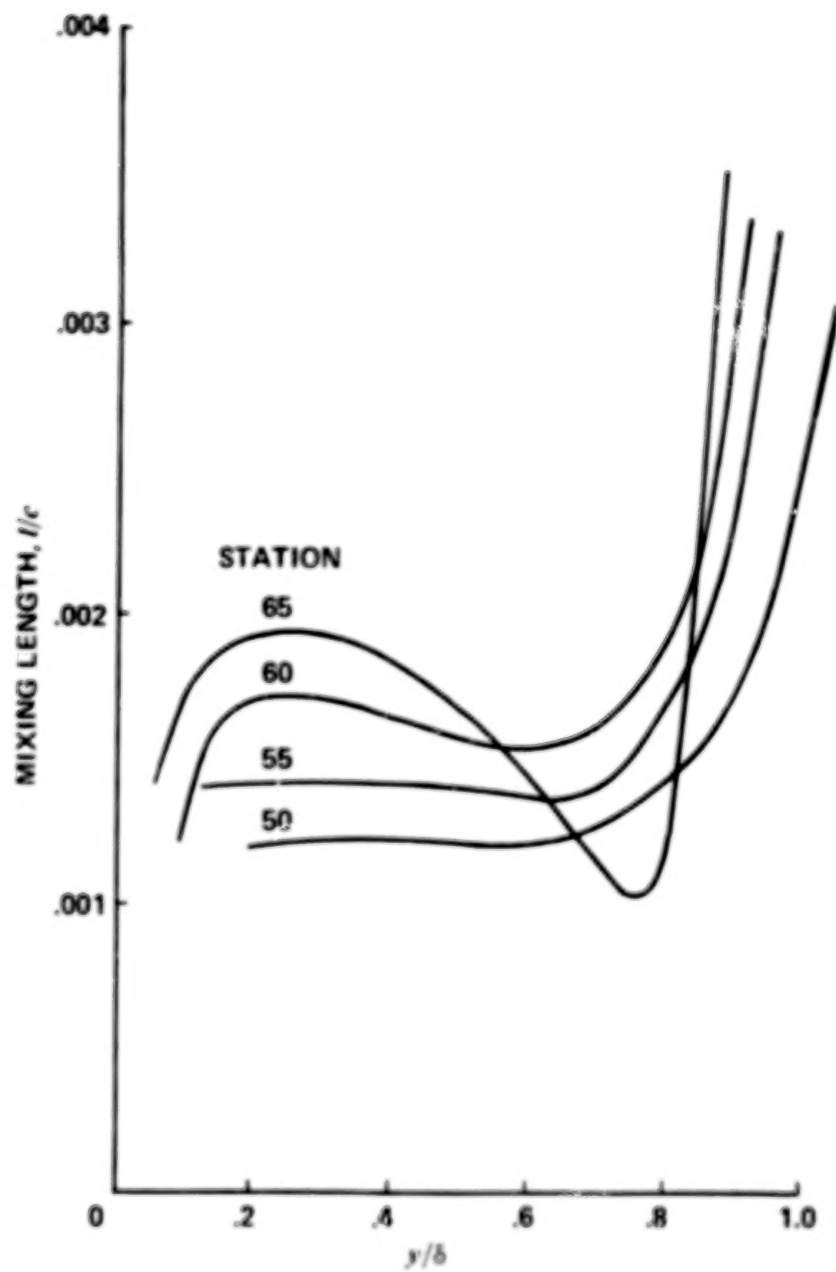
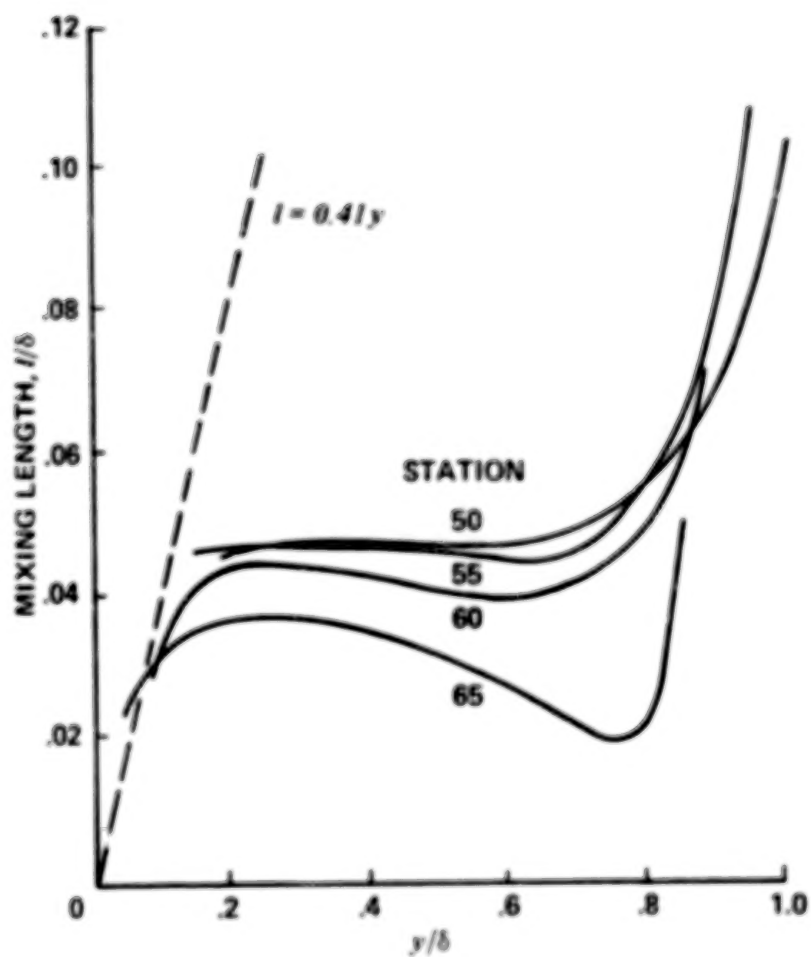Figure 36. Variation of mixing length through attached boundary layer.

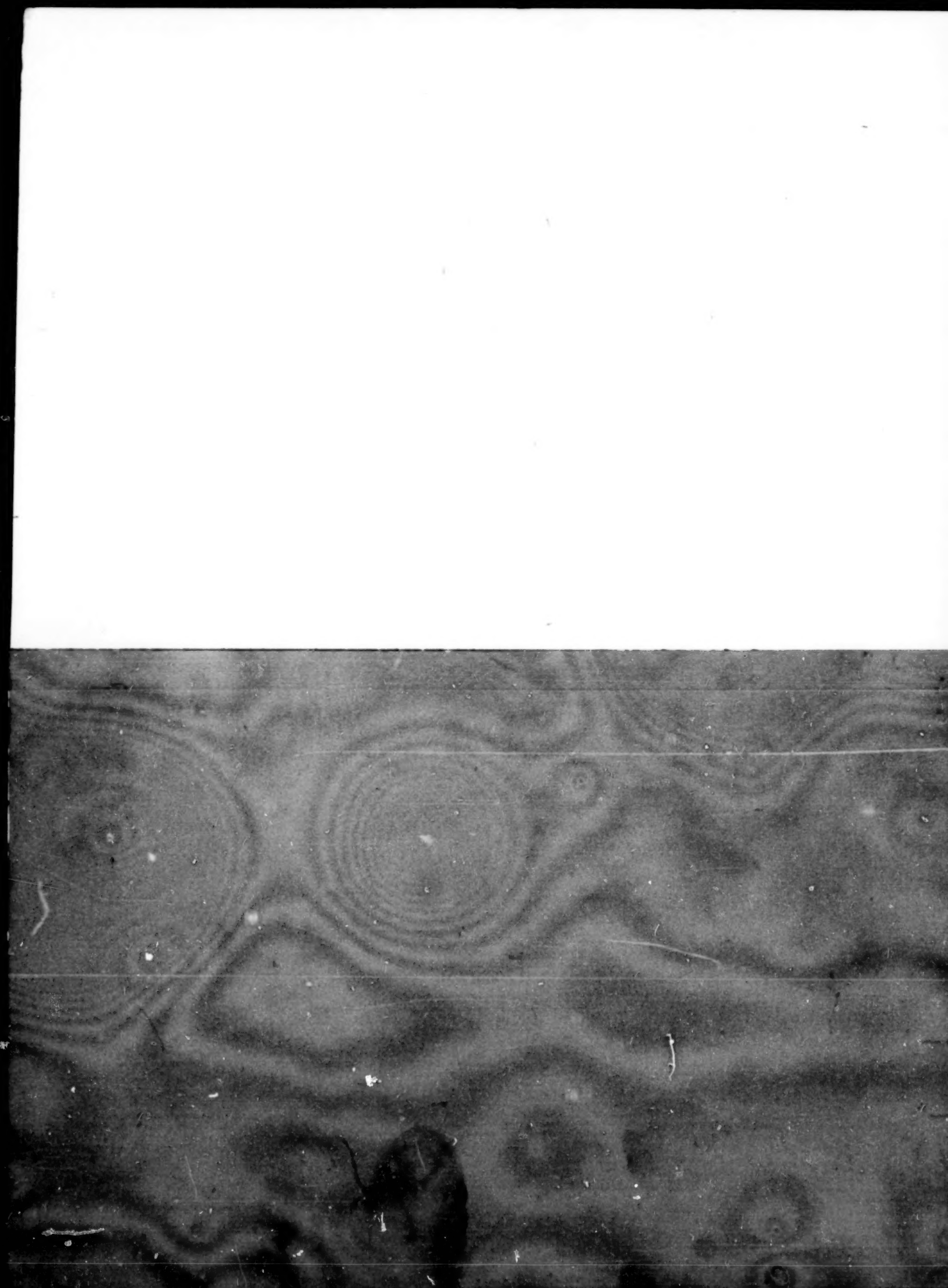Figure 37. Variation of mixing length through attached boundary layer.

1. Report No. NASA CR-3283	2. Government Accession No.	3. Recipient's Catalog No.

4. Title and Subtitle	5. Report Date May 1980
Simple Turbulence Models and Their Application to Boundary Layer Separation	6. Performing Organization Code

7. Author(s) Alan J. Wadcock	8. Performing Organization Report No.

9. Performing Organization Name and Address	10. Work Unit No.
Beam Engineering, Inc. 732 North Pastoria Avenue Sunnyvale, CA 94086	11. Contract or Grant No. NAS2-10093

12. Sponsoring Agency Name and Address	13. Type of Report and Period Covered Contractor Report
National Aeronautics and Space Administration Washington, D. C. 20546	14. Sponsoring Agency Code

15. Supplementary Notes

Ames Technical Monitor: Lawrence E. Olson
Final Report

16. Abstract

Measurements in the boundary layer and wake of a stalled airfoil are presented in two coordinate systems - one aligned with the airfoil chord, the other being conventional boundary layer coordinates. The NACA 4412 airfoil is studied at a single angle of attack corresponding to maximum lift, the Reynolds number based on chord being 1.5×10^6. Turbulent boundary layer separation occurred at the 85% chord position. The two-dimensionality of the flow was documented and the momentum integral equation studied to illustrate the importance of turbulence contributions as separation is approached. The assumptions of simple eddy-viscosity and mixing-length turbulence models are checked directly against experiment. Curvature effects are found to be important as separation is approached.

17. Key Words (Suggested by Author(s))	18. Distribution Statement
Airfoil, Turbulence Modeling, Separated Flow, Boundary Layer, Turbulence	Distribution - Unlimited Star Category - 02

19. Security Classif. (of this report) Unclassified	20. Security Classif. (of this page) Unclassified	21. No. of Pages 67	22. Price* $5.25

END

June 18, 1981